Tidal Effects on the Longitudinal Structures of the Martian Thermosphere and Topside Ionosphere Observed by MAVEN

Xiaohua Fang [1], Jeffrey M. Forbes [2], Quan Gan [1], Guiping Liu [3], Scott Thaller [1], Stephen Bougher [4], Laila Andersson [1], Mehdi Benna [5], Francis Eparvier [1], Yingjuan Ma [6], David Pawlowski [7], Scott England [8], and Bruce Jakosky [1]

[1]Laboratory for Atmospheric and Space Physics, University of Colorado, Boulder, Colorado, USA
[2]Ann and H.J. Smead Department of Aerospace Engineering Sciences, University of Colorado, Boulder, Colorado, USA
[3]Space Sciences Laboratory, University of California, Berkeley, California, USA
[4]Department of Climate and Space Sciences and Engineering, University of Michigan, Ann Arbor, Michigan, USA
[5]NASA Goddard Space Flight Center, Greenbelt, Maryland, USA
[6]Department of Earth, Planetary and Space Sciences, University of California, Los Angeles, California, USA
[7]Physics and Astronomy Department, Eastern Michigan University, Ypsilanti, Michigan, USA
[8]Department of Aerospace and Ocean Engineering, Virginia Polytechnic Institute and State University, Blacksburg, VA, USA

Key Points:

- Direct observational evidence for Martian thermosphere-ionosphere coupling by atmospheric tides is presented.
- The ionosphere below 200 km altitude is controlled by photochemistry and modulated by tide-induced vertical displacement.
- Atmospheric tides constitute a ubiquitous, significant source of ionospheric electron density variability (up to ∼15% at 200 km altitude).

Corresponding author: Xiaohua Fang, Xiaohua.Fang@lasp.colorado.edu

This is the author manuscript accepted for publication and has undergone full peer review but has not been through the copyediting, typesetting, pagination and proofreading process, which may lead to differences between this version and the Version of Record. Please cite this article as doi: 10.1029/2020JA028562.

Abstract

Longitudinal structures in the Martian thermosphere and topside ionosphere between 150-200 km altitudes are studied using in-situ electron and neutral measurements from the NASA Mars Atmosphere and Volatile EvolutioN (MAVEN) mission. Four time intervals are selected for comparison, during which MAVEN sampled similar local time (9.3-10.3 h) and latitude (near 20°S) regions but at different solar longitude positions (two near northern summer solstice, one each at northern vernal and autumnal equinoxes). Persistent and pronounced tidal oscillations characterize the ionosphere and thermosphere, whose longitudinal variations in density are generally in-phase with each other. Our analysis of simultaneous and collocated neutral and electron data provides direct observational evidence for thermosphere-ionosphere coupling through atmospheric tides. We conclude that the ionosphere is subject to modulation by upward-propagating thermal tides, via both tide-induced vertical displacement and photochemical reactions. Atmospheric tides constitute a ubiquitous and significant perturbation source to the ionospheric electron density, up to ∼15% near 200 km.

Plain Language Summary

Vertically-propagating tides are a type of global-scale periodic oscillation caused by solar heating in a rotating planetary atmosphere. Martian atmospheric tidal waves have been extensively observed and studied at low altitudes, but our knowledge concerning their behavior at high altitudes is sparse. In particular, little is known about tidal oscillations in the ionosphere, which is the part of the upper atmosphere that is ionized by absorption of solar EUV and X-ray irradiance. Using in-situ neutral and electron measurements from the NASA Mars Atmosphere and Volatile EvolutioN (MAVEN) mission, we investigate thermal tidal signatures in both the Martian upper atmosphere and ionosphere. Our analysis of simultaneous and collocated ionospheric and atmospheric data provides direct observational evidence that the charged and neutral regimes are tightly coupled, not only through well-understood photochemical reactions but also by tidal waves forced from below. This study elucidates the role of planetary-scale tidal waves in coupling various elements of the near-Mars space environment. Besides our directly-examined neutral-electron density coupling, this study also sheds light on the nature of vertical coupling between the lower and upper atmospheric regimes of Mars.

1 Introduction

Atmospheric tides play an important role in vertical coupling between Martian lower and upper atmospheres. Longitudinal variation of the tidal spectrum is mainly controlled by the planet's topography (e.g., Zurek, 1976; Moudden & Forbes, 2008), which modulates the near-surface heating due to infrared (IR) radiation absorption by CO_2. Observational evidence for vertical coupling by tides in the atmosphere is mainly provided by temperature measurements between 20-80 km altitudes from Mars Reconnaissance Orbiter (MRO) (e.g., Guzewich et al., 2012; Wu et al., 2015), and by accelerometer measurements of total mass density between 95-160 km from Mars Global Surveyor (MGS), Mars Odyssey, and MRO (e.g., Wilson, 2002; Withers et al., 2003; Wang et al., 2006; Bougher et al., 2017; Forbes & Zhang, 2018). The study of atmospheric tidal structures at 120-200 km altitudes has recently been enabled by the Mars Atmosphere and Volatile EvolutioN (MAVEN) mission, using its in-situ measurements from the Neutral Gas and Ion Mass Spectrometer (NGIMS) instrument and remote sensing data from the Imaging UltraViolet Spectrograph (IUVS) instrument (Lo et al., 2015; England et al., 2016; Liu et al., 2017; England et al., 2019; Thaller et al., 2020). Supporting theoretical and modeling studies also have been performed (e.g., Forbes et al., 2002, 2020; Wilson, 2002; Moudden & Forbes, 2008).

Not only upper atmospheres, but also ionospheres, are subject to the modulation of atmospheric tides that are forced from below. For Earth, atmospheric solar tides originating near the surface influence the longitudinal structure of the ionosphere (e.g., Immel et al., 2006; Hagan et al., 2007) through dynamo-generated electric fields in the E-region (100-150 km), which are then mapped upward along magnetic field lines to the F-region (200-500 km). As a result, $\mathbf{E}\times\mathbf{B}$ drifts redistribute plasma in a way that reflects the longitude dependence of the tidal spectrum. Unlike Earth, Mars has no intrinsic dipole magnetic field, but instead localized crustal magnetic anomalies. To date, no evidence exists to support crustal magnetic field influences on tidal oscillations.

Our knowledge of ionospheric tidal structures at Mars is remarkably sparse except for a handful of previous studies. Using MGS radio occultation measurements over northern high latitudes near aphelion, Bougher et al. (2001) found strong longitudinal wave-3 oscillations in the ionospheric peak altitude, consistent with those of atmospheric mass density from MGS accelerometer experiments. However, the ionosphere and atmosphere

were not sampled at the same place but 12 hours apart in local time (LT). Using more MGS data, Bougher et al. (2004) reported interannual repeatability in wave features of the ionospheric peak altitude during aphelion conditions in two Martian years. Under similar seasonal and latitudinal conditions, Cahoy et al. (2006) analyzed MGS-derived atmospheric refractivity within 0-250 km altitudes, which reflected neutral and electron densities below and above ∼75 km altitude, respectively. Their results suggested that upward-propagating solar asynchronous tides were responsible for the observed ionospheric longitudinal structure. The oscillation amplitude of the ionosphere could be replicated by applying a thermal-tide-induced vertical displacement to zonal-mean ionospheric altitude profiles.

Tide-induced coupling between the Martian ionosphere and thermosphere (IT) is plausible but lacks direct observational evidence thus far. Simultaneous and collocated atmospheric and ionospheric tidal observations were unavailable in the pre-MAVEN era. The advantage of direct in-situ measurements by MAVEN, over indirect atmospheric density estimation by accelerometers and non-collocated ionospheric remote sounding by radio occultations, includes the reduction of uncertainties and errors due to assumptions made in indirect approaches. Our work is undertaken to fill in the important knowledge gap in I-T coupling at Mars.

2 MAVEN Data

MAVEN has an elliptical orbit with a period of 3.6-4.6 hours, routinely sampling the atmosphere and ionosphere near periapsis (∼150 km). We use in-situ neutral measurements by MAVEN NGIMS (Mahaffy et al., 2015; Benna et al., 2015) and in-situ electron measurements by the MAVEN Langmuir Probe and Waves (LPW) instrument (Andersson et al., 2015). The NGIMS-derived abundances of CO_2, O, N_2, and Ar, which are representative constituents of the upper atmosphere, are analyzed. Of these, CO_2 and O are the main neutral species at low and high altitudes, respectively, and are the most important participants in the photochemical reactions in the Martian ionosphere. In addition, CO_2, N_2, and Ar are nonreactive species and therefore their longitudinal variations are good indicators of the tidal structures of the atmosphere. The data utilized for this work include only inbound data for both instruments and with a high confidence level: NGIMS data with a quality flag of "IV" (an abbreviation for inbound and verified) and LPW data with a quality flag of >50. Exclusion of the outbound NGIMS data

is to avoid potential adhesive contamination. As inbound and outbound segments span different latitudes, outbound LPW data are excluded to ensure that collocated I-T structures are compared. For the NGIMS instrument, we use level 2, version 8, revision 1 data for this work.

Figure 1 shows the projections of inbound orbits within 150-200 km altitude on the LT-latitude plane, color coded by time. The upper limit altitude of 200 km is imposed to ensure reliable retrieval and statistical analysis of tidal signatures, given that there are considerably fewer in-situ measurements at the higher altitudes (see the supporting information, SI, for the MAVEN data coverage). Moreover, non-tidal dynamic processes become important at high altitudes and contribute increasing "noise" to our tidal analysis. For example, the altitude of 200 km is an approximate transition altitude for the ionosphere, above which it departs from photochemical equilibrium and is subject to the control of plasma transport. The MAVEN orbit is designed such that it slowly and continuously precesses in both LT and latitude. Figure 1 indicates that there are compatible LT-latitude regions sampled by MAVEN several times, out of which we examine the four highlighted near-noon (between 9.3-10.3 h in LT) and near-equator (near 20°S) passages in the southern hemisphere. The constraint of the 1-h LT window facilitates the tidal investigation by avoiding a mixture of different phases. In addition, the LT restriction also imposes a restriction on latitude (Figure 1a), efficiently excluding the mixture of latitude-varying tidal signatures.

Table 1 summarizes the four cases examined in this work. The data sets are ordered by their positions in solar longitude (Ls, as a proxy of season): Ls1 (centered at Ls=63°), Ls2 (94°), Ls3 (177°), Ls4 (340°). As seen in Figure 1b, Ls1 and Ls2 correspond to the aphelion and northern summer season (straddling the aphelion point of Ls=71°), Ls3 is for the northern autumnal equinox, and Ls4 occurs near the northern vernal equinox. Ls1 and Ls2 are separated by 1 Martian year, and their differences may shed light on interannual variations. Solar irradiance upon the Martian atmosphere is the main driver of thermal tides and is also included in Table 1. Comparison of the inverse square of the Sun-Mars distance shows that during equinox (cases Ls3, Ls4) Mars receives 27% more solar IR radiation than at aphelion (cases Ls1, Ls2). Particular attention is paid to solar extreme ultraviolet (EUV) radiation, which supplies primary heating for the upper atmosphere and is the dominant photoionization source for the ionosphere. MAVEN carries a dedicated solar irradiance instrument: EUV Monitor, EUVM (Eparvier et al., 2015).

Specifically, its channel-A covers the 17-22 nm wavelength portion of solar EUV. The other two EUVM channels (B an C, covering soft X-ray and Lyman-alpha wavelengths, respectively) are not directly relevant. As given in Table 1 and also the SI, the mean 17-22 nm EUV energy flux in Ls1 at Mars is greater by 68% than in Ls2, and the Ls4 intensity is greater by 75% than in Ls3. The extrapolated $F_{10.7}$ index at Mars differs by ∼50% between Ls1 and Ls2 and between Ls3 and Ls4. Therefore, atmospheric and ionospheric responses in Ls1-Ls4 are mixed by seasonal and solar EUV effects. In addition, the four cases correspond to different dust activities. In this study, we use the column dust optical depth at the wavelength of 9.3 μm to describe the dust loading level in the atmosphere (cf., Montabone et al., 2020; Fang et al., 2020). As seen from dust opacities in Table 1 and the SI, significant atmospheric dust loading happens in Ls3 and Ls4, while Ls1-Ls2 are in the low-dust-loading season and basically dust-free.

3 Tides and Longitudinal Structure

The interaction between solar heating and topography on a rotating planet results in periodic dependencies on time and longitude. Solar tides are mathematically expressed as

$$\sum_n \sum_s A_{n,s}(z,\theta)\cos(n\Omega t + s\lambda - \phi_{n,s}(z,\theta)), \tag{1}$$

where t is universal time, $\Omega = 2\pi \mathrm{sol}^{-1}$, z is altitude, λ is longitude, θ is latitude, integer n defines the oscillation frequency, integer s is the zonal wavenumber, $A_{n,s}$ is amplitude, and $\phi_{n,s}$ is phase. Negative and positive values of s correspond to eastward-propagating and westward-propagating waves, respectively. Tides with $s = 0$ do not propagate zonally and are called zonally-symmetric. The notation DWs or DEs is used to denote a westward or eastward-propagating diurnal tide, respectively, with zonal wavenumber of s. For semidiurnal oscillations, 'S' replaces 'D'. The zonally-symmetric oscillations are denoted D0, S0.

Expressed in terms of local time (t_{LT}), equation (1) becomes

$$\sum_n \sum_s A_{n,s}(z,\theta)\cos(n\Omega t_{LT} + (s-n)\lambda - \phi_{n,s}(z,\theta)). \tag{2}$$

Therefore, tidal signatures in satellite data from quasi-sun-synchronous orbit (LT ≈ constant, which is the case in our study) are manifested in terms of longitudinal variations, specifically their space-based wavenumber $k_s = |s - n|$. However, there is ambiguity

inherent in these signatures, since multiple combinations of s and n may yield the same k_s. From basic tidal theory and the tidal simulations of Forbes et al. (2002) which extend to 200 km altitude, the set of reasonable choices for the major contributors in the Martian thermosphere region above 150 km were thought to include D0 and SW1 for k_s=1, DE1 and S0 for k_s=2, and DE2 and SE1 for k_s=3.

In this study, MAVEN data are sorted into 30°-longitude and 5 km-altitude bins. As the analysis is conducted at the center of bins, the maximum 2.5 km vertical distance from bin centers to edges, which corresponds to ∼0.25 scale heights of neutral densities and ∼0.1 scale heights of electron densities, ensures a reasonable altitude resolution. In order to remove outliers, only data points between 10th-90th percentiles inside each bin are used for averaging. Least-squares harmonic fits are performed independently at altitude levels wherever data coverage is available over all the 12 longitude bins. Consistent with the longitude resolution, spectral fits are limited to wavenumbers k_s=1-3.

For the neutral species, we first examine CO_2, which is the major constituent. Figures 2-5 show the MAVEN spatial coverage of CO_2 and electron densities and their longitudinal structures in Ls1-Ls4, respectively. Through the constraints on local time and altitude, the latitudinal span is considerably narrowed. A well-spread longitude sampling naturally results from Mars rotation beneath MAVEN's orbit. Differences in the spatial coverages of NGIMS and LPW data are due to separate data selection criteria adopted for the two instruments. The longitudinal structures of CO_2 and electron densities show an overall agreement in their periodic features. Taking Ls1 as an example (see Figure 2), prominent local ridges are seen near 120°W, 0°, and 120°E longitudes in this case, although longitudinal shifts are observed with altitude and between CO_2 and electron densities. Near 160-km altitude, the trough-to-peak altitude variations for the contours of 5×10^8 cm^{-3} CO_2 density (Figure 2c) and 3×10^4 cm^{-3} electron density (Figure 2i) are about 6 km and 8 km, respectively. It is worth noting that the wave fits and decompositions are independently performed at individual altitude levels and are based on the independent instrument data sets for neutrals and electrons. The overall consistency in longitude positions of wave troughs and ridges, within the entire examined altitude range and between the thermosphere and ionosphere, confirms that the obtained longitudinal structures capture real tidal signatures and are unlikely attributable to data noise or other known causes.

Two potentially significant factors need to be considered when analyzing the Martian ionosphere. One is solar zenith angle (SZA), which is a key parameter in determining the ionospheric peak altitude and strength. Nevertheless, given that the altitudes of interest in this study are above ionospheric peak altitudes by at least several neutral scale heights, the ionospheric variability within the limited SZA ranges on the dayside (Table 1) are indeed negligible according to Chapman theory (cf. Schunk & Nagy, 2009) and also our detailed analysis included in the SI. The other factor is the possible influence of Mars' crustal magnetic anomalies (e.g., Andrews et al., 2015; Fang et al., 2015, 2017). The longitude-latitude projections of the MAVEN orbits (as included in the SI) show that strong crustal magnetic field regions are avoided in our cases. No apparent anomalies in electron density are found in Figures 2-5 in the near-180° longitude bins, where the crustal field is locally concentrated and has a much stronger strength than elsewhere.

The detailed longitudinal decompositions at three representative altitudes in Figures 2-5 unveil the constructive and destructive interference effects of k_s=1-3 wave components. For example, in Ls1 (Figure 2), wave-3 is predominant over the altitude range for both CO_2 and electrons, except below ~160 km where the wave-2 component becomes comparable for electrons and even dominant for CO_2. Wave-1 makes the least contribution to the tidal oscillations of CO_2 and electrons except near 200 km altitude, where it may exceed wave-2 but is generally weaker than wave-3. Despite the general consistency in longitudinal structure between CO_2 and electron densities, there is a distinct difference in terms of the amplitude in percent deviation from the mean. In Ls1, the three wavenumber amplitudes of electron density variation at the central altitude of 180 km are about 1/2 of the counterparts for the CO_2 density variation, and the ratio changes with altitude and drops to ~1/3 at higher and lower altitudes.

The apparently weaker tidal signatures in the ionosphere in Ls1 may be simply accounted for by the combined effects of thermal-tide-induced vertical displacement and photochemistry. We consider the classic Chapman approximation, in which the ionosphere is produced by monochromatic solar EUV photoionization of an isothermal, single-species atmosphere. The neutral density $n_n(z)$ exponentially decreases with a constant hydrostatic scale height of H_n, where the subscript 'n' denotes neutral constituents. The ionospheric density peaks at the altitude of unit optical depth, above which the density exponentially decreases with altitude following a scale height of $H_e \approx 2H_n$ (cf. Schunk & Nagy, 2009). Note that the altitude region considered in this study is sufficiently high

above the ionospheric peak. The scale height doubling in the topside ionosphere is determined by the photochemical equilibrium between photoionization and recombination loss, the latter of which is proportional to the electron density squared. For a vertical displacement of δh induced by thermal tides, the resulting perturbation in the neutral density is given by

$$\delta n_n(z) = n_n(z - \delta h) - n_n(z) = -\frac{dn_n(z)}{dz}\delta h = \frac{n_n(z)}{H_n}\delta h. \tag{3}$$

Rearranging equation (3) and likewise for the topside ionosphere, we obtain their normalized perturbations as

$$\begin{aligned} \frac{\delta n_n}{n_n} &= \frac{\delta h}{H_n}, \\ \frac{\delta n_e}{n_e} &= \frac{\delta h}{H_e} \approx \frac{1}{2}\frac{\delta n_n}{n_n}. \end{aligned} \tag{4}$$

That is, tidal variations in a Chapman ionosphere are predicted to be about half of those in the neutral atmosphere.

Actual conditions are far more complicated than accounted for by Chapman theory. Including all important neutral and ion species and chemical reactions, the numerical simulation of Fang et al. (2020) illustrates that the vertical profile of ionospheric electron densities (or total ion densities) approximately moves as a whole in accordance with dust-storm-induced upper atmospheric expansion, even though individual ion species react differently in response to neutral compositional changes. This supports the inherent assumption in equation (4) that the vertical displacement imposed by thermal tides transfers from thermospheric main neutral constituents to ionospheric electrons to a similar extent through photochemical reactions; that is, $(\delta h)_n$ and $(\delta h)_e$ are comparable to each other. However, as seen in Figures 2-5, deviations from the nominal "1/2 rule" are observed at different altitudes and under various conditions. Our calculation shows that the normalized wave amplitudes for variations of electron, CO_2, O, N_2, and Ar densities are 8.1±4.3%, 12.4±6.7%, 16.4±6.2%, 10.7±4.4%, 10.1±4.6%, respectively. These values represent the average and one standard deviation over all the examined altitudes and wave components within the four cases, showing a significant scatter. As a result, the ratios of the average electron wave amplitude to those of the neutrals are 0.65 (electron vs. CO_2), 0.50 (electron vs. O), 0.76 (electron vs. N_2), 0.81 (electron vs. Ar). That is, except that the ratio of the average tidal variation of electron density to that of the O density coincides with the prediction of simplistic Chapman theory, the amplitude ratios of the electron to the other neutral species are larger than 0.5 but less than 1. One

caution to be noted is that the altitude variation of the amplitudes is not smooth (which is in part because the wave fits are independently performed on an altitude-by-altitude basis here), leading to a larger-than-one ratio between electron and neutral amplitudes at some altitudes. Nevertheless, generally speaking, tidal variations in electron density are weaker than those of thermospheric neutral densities. The complexity of the tidal wave distributions and their comparisons between charged and neutral particles reflects the fact that complex photochemical reactions are present in reality and the tide-induced vertical displacement of δh varies not only in space but also with atmospheric species. For example, deviations from the simplistic relationship of $H_e \approx 2H_n$ actually prevail in the upper ionosphere (e.g., Němec et al., 2011). Furthermore, the constructive and destructive interactions of tidal components, which may be associated with different vertical displacements (Cahoy et al., 2006), come into play in regulating zonal variations. The tidal structures at three representative altitudes of 160 km, 180 km, and 200 km in Ls1-Ls4 are characterized in Table 2 and also presented in Figure 6.

It is seen in Figure 6 that the thermospheric tidal structures are complex and species dependent: the atomic oxygen density overall has large wave amplitudes in comparison with the dominant species CO_2 and other species like N_2 and Ar, although the opposite may be expected from equation (4) given the larger scale height for the zonal mean O density (see Table 2). Our observation of the relatively larger amplitudes for O disagrees with England et al. (2016), who reported a correlation between wave amplitudes and inverse scale heights of neutrals (H_n^{-1}) among the neutral species (including O). Different analysis approaches and different observational conditions in terms of Ls, LT, and latitude cause great difficulties in interpreting the discrepancy between the current study and the previous one. One explanation is that atmospheric O behaves differently in our cases (for example, possibly having a greater vertical displacement than other neutral species in equation 4), while the tide-induced vertical displacement is comparable among all neutral species in the cases of England et al. (2016) such that the wave amplitude is mainly determined by the scale height. Although the correlation between the wave amplitude and H_n^{-1} is observed in some scenarios in Figure 6, we also see apparent inconsistencies with this approximation in other scenarios, for example, for K_s=1 at 200 km altitude in Ls3 (see red symbols).

Figure 7 compares Ls1-Ls4 longitudinal wave components of thermospheric CO_2 and O densities and ionospheric electron density and temperature. A prominent feature

is that tidal signatures, which exist in the zonal variations for both neutrals and electrons, are manifested as persistent and pronounced waves 1-3. The longitudinal phases within each case reasonably agree between the thermosphere and ionosphere. In all cases, the longitudinal variability of the neutral constituents of CO_2, O, N_2, and Ar show important k_s=1-3 waves. However, in the equinox seasons (Ls3, Ls4), the importance of the k_s=1 component is greatly enhanced for the minor species of O, having an amplitude comparable to or even larger than the higher-wavenumber components. Unlike CO_2 that is in diffusive equilibrium, the variability of O is also significantly subject to the effects of winds and day-to-night transport by the diurnal circulation system, probably because the wind-induced diffusion impacts light species but not CO_2 (Bougher et al., 2015). It remains unclear how O responds to temperatures, vertical and horizontal winds imposed by vertically-propagating tides. The comparison between CO_2 and O variations induced by tides within the current data set thus provides valuable new constraints for models.

These amplitude variations with altitude seem not to conform to theoretical expectations for vertically-propagating tides in a diffusion-dominated Mars atmospheric regime. Wave amplitudes were predicted by Forbes et al. (2002) to have a monotonic increase with altitude or to be near-constant. Their numerical results, which employ a simple linear model of tides in the thermosphere, suggest that horizontal winds and temperatures remain approximately constant with altitude above ∼140 km, and that density perturbations monotonically increase with altitude by about a factor of ∼2 between 140 and 200 km. In contrast, MAVEN data in Figure 7 show a more complex picture than that, including abrupt phase transitions. In principle, irregular amplitude and phase behaviors are introduced when multiple tidal components with different phase progressions with altitude are present, and this could potentially be exacerbated by temporal variability of these components by, e.g., planetary wave modulation (Moudden & Forbes, 2010). Our approach here is not to focus on the absolute vertical amplitude and phase structures, but instead on altitude-longitude structures of relative amplitudes to meet our overall objective of elucidating thermospheric and ionospheric tidal modulations from the I-T coupling perspective.

Figure 7 illustrate that the ionospheric electron densities in all the cases are subject to significant modulation by thermal tides: k_s=1-3 wave amplitudes increase (non-monotonically) from ∼5% at 150 km altitude up to ∼15% at 200 km. The ionospheric

tidal signatures are generally weaker compared with the neutral species, albeit some exceptions as seen in Figure 7. Note that the electron density k_s=1 component prevails upon the other higher-wavenumber components in longitudinal structure during the equinox seasons of Ls3 and Ls4, which coincides with the similar dominance for neutral O. This coincidence highlights the role of photochemical reactions in ionospheric formation and tidal modulations, in which atomic O plays a crucial role in converting CO_2^+ into the main ion species O_2^+. Abrupt phase shifts in n_e tidal signatures happen at around 180-190 km altitudes, where the ionosphere starts to deviate from photochemical equilibrium due to the increasing importance of plasma transport.

Several features stand out in Figure 7 and Table 2 regarding the electron temperature, T_e. First, the tidal oscillation of T_e is very weak, with wave amplitudes mostly less than 5%. Second, T_e shows generally opposite phasing from n_e in terms of their longitudinal structures, that is, with a nearly 180° shift. This can be simply explained using the Chapman approximation. Because of the generality, equation (3) can be reasonably extended so that in association with a tide-induced vertical displacement, the sign of the slope for a physical parameter directly controls the sign of its tidal perturbation. It is known that n_e in the topside ionosphere has a trend consistent with neutral densities (i.e., $dn_e/dz < 0$) but opposite against T_e (i.e., $dT_e/dz > 0$) (e.g., Hanson et al., 1977; Sakai et al., 2016). It can be inferred that a vertical displacement by thermal tides would result in consistent phasing in longitudinal variation between thermospheric and ionospheric densities but opposite phasing between n_e and T_e. An exception to this is observed in Ls4, where n_e and T_e show comparable tidal phases. One probable cause is that Ls4 took place during a regional dust storm season (see Table 1 and SI). Dust storms are an important driver in the Martian lower atmosphere and their effects are seen up into the upper atmosphere, ionosphere, and even magnetosphere (e.g., Fang et al., 2020, and references therein). It is known that dust storms cause disturbances to lower atmospheric heating, circulation, and coupling with the upper atmosphere, and tidal behaviors under dusty conditions would also be greatly altered (e.g., Leovy & Zurek, 1979; Forbes & Miyahara, 2006).

Figure 8 shows the altitude variation of the normalized k_s=1-3 amplitudes for the thermosphere (including CO_2, O, N_2, and Ar densities) and for the ionosphere (electron density and temperature). The zonal means, which are used to normalize the amplitudes, are also shown. As discussed above, ionospheric electron densities are subject to signif-

icant modulation by thermal tides, with k_s=1-3 wave amplitudes increasing from ∼5% at 150 km altitude up to ∼15% at 200 km. The tidal oscillation in the ionospheric electron density is on average weaker than that in the thermosphere. The tidal impact on the electron temperature is even weaker, basically less than 5%. The thermospheric tidal structures are complex and show a species dependence: the atomic oxygen density overall has large wave amplitudes in comparison with the dominant species CO_2 and other species like N_2 and Ar, although the zonal mean O density has a larger scale height. The differences among Ls1-Ls4 we see in Figure 8 reflect not only seasonal effects but also solar activity effects (see also Table 1). Even though the Sun-Mars distance is nearly identical between Ls1 and Ls2 and between Ls3 and Ls4, the overhead solar EUV levels in Ls1 and Ls4 are $> 50\%$ stronger than Ls2 and Ls3, respectively. Such a combined effect also manifests itself in controlling the zonal mean density profile (see the leftmost column of Figure 8). For instance, while the zonal mean CO_2 densities in the Ls3-Ls4 (equinox) group are greater than those in the Ls1-Ls2 (aphelion) group, we note that the densities in Ls1(Ls4) are greater than those in Ls2(Ls3) by a factor of ∼2 at 175 km altitude, consistent with the difference in solar EUV. The differences in zonal-mean profiles directly affect tidal wave propagation and dissipation. However, on the other hand, thermal tides propagating upward from the lower atmosphere have an impact on the zonal mean circulation and density and temperature structure of the upper atmospheric region. Disentangling the interplay between seasonal and solar EUV effects awaits future studies when more cases under distinctly different Ls and EUV conditions are available.

4 Comparison with the Mars Climate Database

In the recent work of Forbes et al. (2020), the tidal spectrum at 76 km above Mars surface as a function of latitude and Ls was derived from MRO Mars Climate Sounder observations, and found to agree well with the results of the Mars Climate Database (MCD). MCD provides predictions from the Laboratoire de Meteorologie Dynamique (LMD) Global Climate Model (Forget et al., 1999; González-Galindo et al., 2015). The MCD was used to predict density variability at Mars thermospheric altitudes and to understand the physical processes that affect the vertical propagation of tides from lower altitudes. The MCD also captured well the salient amplitude and phase characteristics of the longitudinal density perturbations (∼ ±30-60%) measured by the MGS accelerometer.

The ability of the MCD to capture the tidal spectrum at 76 km and self-consistently the density variability near 110 km suggests that the MCD can serve as a credible source for interpretation of the MAVEN density variability examined in this study. Therefore, we retrieved from Figures 10 and 11 of Forbes et al. (2020) various tidal contributions to total mass density at 172 km as predicted by the MCD, which are summarized in Table 3. These MCD results are compared with the MAVEN wavenumber 1-3 amplitudes (A_1, A_2, A_3) for CO_2 at 180 km in Table 2. This comparison aims to provide crude guidance to the tidal interpretation of the MAVEN data, considering that (a) the MCD model is climatological; (b) some shortcomings in the model still exist; and (c) phase differences between individual contributions to a vector sum wavenumber amplitude will result in diminished total amplitudes compared to the arithmetic sum of amplitudes. With these caveats in mind, the individual contributions of stationary planetary wave with s=1 (SPW1) and D0 to wave-1 in the MCD are of order 3-7%, and can plausibly account for the observed amplitudes except during Ls2 when A_1=17%. For A_2, DE1 (6-13%), SPW2 (2-4%) and S0 (4%) occur within ranges of amplitudes that when combined can account for the MAVEN amplitudes, except perhaps A_2=16.6% during Ls3. Moreover, DE2 (12-16%), SE1 (4%) and SPW3 (3-6%) appear capable of accounting for the range of A_3 amplitudes observed by MAVEN.

The list of tides above is not too different than those quoted in connection with the work of Forbes et al. (2002) in the previous section except for the absence of SW1, and the addition of SPW1, SPW2 and SPW3. SW1 amplitudes in the MCD at 172 km are generally less than 4% at all latitudes and Ls, and were not included in the interpretation of MAVEN data in Table 2. The non-negligible (5-8%) contributions of SPW1, SPW2, and SPW3 in the MCD represented a new revelation, and were interpreted by Forbes et al. (2020) as by-products of tide-tide nonlinear interactions in the Martian thermosphere.

The Forbes et al. (2020) work was based on the MCD climatologies for average solar conditions. The tidal density perturbations (relative to the zonal mean) above 100 km were subsequently recalculated for minimum solar activity conditions, and were found to differ little in amplitude and structure from those corresponding to average solar conditions. This result confirms the intuitive expectation that taking density perturbations relative to the zonal mean essentially removes the dependence on solar activity, and supports the choice to analyze relative density perturbations in the current study.

5 Conclusions

The longitudinal structures of the Martian thermosphere and topside ionosphere are investigated within 150-200 km altitude, using simultaneous and collocated MAVEN in-situ neutral and electron measurements. Four time intervals, during which MAVEN sampled compatible local time (9.3-10.3 h) and latitude (near 20°S) regions but at different Ls positions (centered at 63°, 94°, 177°, 340°), are selected for investigation and intercomparison. Our findings are summarized as follows.

1. Longitudinal structures of Martian thermosphere and ionosphere densities show persistent and pronounced wavenumber 1-3 components. Their longitudinal variations are generally in-phase with each other, providing direct observational evidence of I-T coupling through atmospheric tides.
2. The tidal wave variations in the thermospheric CO_2, O, N_2, and Ar densities show important longitudinal wave-1, wave-2, and wave-3 components. The minor neutral species, O, however, shows a different behavior during the equinox seasons. The longitudinal dependence of thermospheric O shows a greatly enhanced wave-1 component in the equinoxes, having an amplitude comparable to or even larger than wave-2 and wave-3 components.
3. Ionospheric electron densities show significant modulation by thermal tides, with wavenumber 1-3 amplitudes increasing (non-monotonically) from ∼5% at 150 km altitude up to ∼15% at 200 km. This underscores the importance of atmospheric tides as a ubiquitous source of ionospheric variability, which has been under-appreciated.
4. The ionospheric tidal signatures in electron density are generally weaker than those of thermospheric neutral densities. The ratios of the relative electron wave amplitude to that of the neutrals range between 0.5 and 0.8 on average, in comparison with the ratio of 0.5 according to the prediction of simplistic Chapman theory.
5. Ionospheric electron temperatures show insignificant tidal signatures, with wave amplitudes of mostly less than 5%. The generally opposite longitude phasing of tidal signatures between the electron density and electron temperature is consistent with the opposite signs of their zonal-mean altitude slopes ($dn_e/dz < 0$ vs. $dT_e/dz > 0$). An exception occurs in the dust storm case, in which comparable

longitude phasing is observed instead. This highlights the potential importance of dust storms in affecting tidal oscillations in the upper atmosphere and ionosphere.

6. The generally consistent longitude phasing in tidal structures between thermosphere neutral densities and ionosphere electron density, as well as the opposite longitude phasing between ionospheric electron density and temperature, are consistent with the picture that the tidal structures of the ionosphere are caused by the combined effects of thermal-tide-induced vertical displacement and photochemical reactions.
7. The zonal-mean densities shown herein suggest that they are subject to some combination of solar and seasonal variability which cannot be disentangled given the limited distribution of the data. On the other hand, the tidal perturbations relative to the zonal mean in the thermosphere, and by extension those in the ionosphere, show little dependence on solar activity in the MCD, and the same is therefore assumed to be true with regard to the longitude variations revealed in the present study.

Acknowledgments

This work was supported by NASA grants 80NSSC19K0562 and NNX16AJ39G and the NASA MAVEN project through the Mars Exploration Program. The authors thank Hanli Liu, Richard Zurek, Roger Yelle, and Xiaoli Zhang for helpful discussions and particularly thank reviewer Daniel Lo for valuable and constructive comments for the improvement of the paper. The MAVEN data are publicly available at NASA Planetary Data System through https://pds.nasa.gov. The column dust optical depth is obtained through the Mars Climate Database project at http://www-mars.lmd.jussieu.fr. The $F_{10.7}$ index and sunspot number are obtained from the OMNI database at https://omniweb.sci.gsfc.nasa.gov/.

References

Andersson, L., Ergun, R., Delory, G., Eriksson, A., Westfall, J., Reed, H., ... Meyers, D. (2015). The langmuir probe and waves (lpw) instrument for maven. *Space Science Reviews*, *195*(1-4), 173–198. doi: 10.1007/s11214-015-0194-3

Andrews, D. J., Andersson, L., Delory, G., Ergun, R., Eriksson, A. I., Fowler, C., ... Jakosky, B. (2015). Ionospheric plasma density variations observed at mars by maven/lpw. *Geophysical Research Letters*, *42*(21), 8862–8869. doi:

doi:10.1002/2015GL065241

Benna, M., Mahaffy, P., Grebowsky, J., Fox, J. L., Yelle, R. V., & Jakosky, B. M. (2015). First measurements of composition and dynamics of the martian ionosphere by maven's neutral gas and ion mass spectrometer. *Geophysical Research Letters*, *42*(21), 8958–8965. doi: 10.1002/2015GL066146

Bougher, S., Brain, D., Fox, J., Francisco, G., Simon-Wedlund, C., & Withers, P. G. (2017). Upper neutral atmosphere and ionosphere. In B. Haberle, M. Smith, T. Clancy, F. Forget, & R. Zurek (Eds.), *The atmosphere and climate of mars* (p. 433-463). Cambridge University Press Cambridge.

Bougher, S., Engel, S., Hinson, D., & Murphy, J. (2004). Mgs radio science electron density profiles: Interannual variability and implications for the martian neutral atmosphere. *Journal of Geophysical Research: Planets*, *109*(E3). doi: doi:10.1029/2003JE002154

Bougher, S., Engel, S., Hinson, D. P., & Forbes, J. M. (2001). Mars global surveyor radio science electron density profiles: Neutral atmosphere implications. *Geophysical Research Letters*, *28*(16), 3091–3094. doi: 10.1029/2001GL012884

Bougher, S., Pawlowski, D., Bell, J., Nelli, S., McDunn, T., Murphy, J., ... Ridley, A. (2015). Mars global ionosphere-thermosphere model: Solar cycle, seasonal, and diurnal variations of the mars upper atmosphere. *Journal of Geophysical Research: Planets*, *120*(2), 311–342. doi: 10.1002/2014JE004715

Cahoy, K., Hinson, D., & Tyler, G. L. (2006). Radio science measurements of atmospheric refractivity with mars global surveyor. *Journal of Geophysical Research: Planets*, *111*(E5). doi: 10.1029/2005JE002634

England, S. L., Liu, G., Kumar, A., Mahaffy, P. R., Elrod, M., Benna, M., ... others (2019). Atmospheric tides at high latitudes in the martian upper atmosphere observed by maven and mro. *Journal of Geophysical Research: Space Physics*, *124*(4), 2943–2953. doi: 10.1029/2019JA026601

England, S. L., Liu, G., Withers, P., Yiğit, E., Lo, D., Jain, S., ... others (2016). Simultaneous observations of atmospheric tides from combined in situ and remote observations at mars from the maven spacecraft. *Journal of Geophysical Research: Planets*, *121*(4), 594–607. doi: 10.1002/2016JE004997

Eparvier, F., Chamberlin, P., Woods, T., & Thiemann, E. (2015). The solar extreme ultraviolet monitor for maven. *Space Science Reviews*, *195*(1-4), 293–301. doi:

10.1007/s11214-015-0195-2

Fang, X., Ma, Y., Brain, D., Dong, Y., & Lillis, R. (2015). Control of mars global atmospheric loss by the continuous rotation of the crustal magnetic field: A time-dependent MHD study. *Journal of Geophysical Research: Space Physics*, *120*(12), 10–926. doi: 10.1002/2015JA021605

Fang, X., Ma, Y., Lee, Y., Bougher, S., Liu, G., Benna, M., ... others (2020). Mars dust storm effects in the ionosphere and magnetosphere and implications for atmospheric carbon loss. *Journal of Geophysical Research: Space Physics*, *125*. doi: 10.1029/2019JA026838

Fang, X., Ma, Y., Masunaga, K., Dong, Y., Brain, D., Halekas, J., ... others (2017). The mars crustal magnetic field control of plasma boundary locations and atmospheric loss: MHD prediction and comparison with MAVEN. *Journal of Geophysical Research: Space Physics*, *122*(4), 4117–4137. doi: 10.1002/2016JA023509

Forbes, J. M., Bridger, A. F., Bougher, S. W., Hagan, M. E., Hollingsworth, J. L., Keating, G. M., & Murphy, J. (2002). Nonmigrating tides in the thermosphere of mars. *Journal of Geophysical Research: Planets*, *107*(E11), 23–1. doi: 10.1029/2001JE001582

Forbes, J. M., & Miyahara, S. (2006). Solar semidiurnal tide in the dusty atmosphere of mars. *Journal of the atmospheric sciences*, *63*(7), 1798–1817.

Forbes, J. M., & Zhang, X. (2018). Polar region variability in the lower thermosphere of mars from odyssey and reconnaissance orbiter aerobraking measurements. *Journal of Geophysical Research: Space Physics*, *123*(10), 8664–8687. doi: 10.1029/2018JA025527

Forbes, J. M., Zhang, X., Forget, F., Millour, E., & Kleinböhl, A. (2020). Solar tides in the middle and upper atmosphere of mars. *Journal of Geophysical Research: Space Physics*, *125*(9), e2020JA028140. doi: 10.1029/2020JA028140

Forget, F., Hourdin, F., Fournier, R., Hourdin, C., Talagrand, O., Collins, M., ... Huot, J.-P. (1999). Improved general circulation models of the martian atmosphere from the surface to above 80 km. *Journal of Geophysical Research: Planets*, *104*(E10), 24155–24175. doi: 10.1029/1999JE001025

González-Galindo, F., López-Valverde, M. A., Forget, F., García-Comas, M., Millour, E., & Montabone, L. (2015). Variability of the martian thermosphere

during eight martian years as simulated by a ground-to-exosphere global circulation model. *Journal of Geophysical Research: Planets*, *120*(11), 2020–2035. doi: 10.1002/2015JE004925

Guzewich, S. D., Talaat, E. R., & Waugh, D. W. (2012). Observations of planetary waves and nonmigrating tides by the mars climate sounder. *Journal of Geophysical Research: Planets*, *117*(E3). doi: 10.1029/2011JE003924

Hagan, M., Maute, A., Roble, R., Richmond, A., Immel, T., & England, S. (2007). Connections between deep tropical clouds and the earth's ionosphere. *Geophysical Research Letters*, *34*(20). doi: 10.1029/2007GL030142

Hanson, W., Sanatani, S., & Zuccaro, D. (1977). The martian ionosphere as observed by the viking retarding potential analyzers. *Journal of Geophysical Research*, *82*(28), 4351–4363.

Immel, T., Sagawa, E., England, S., Henderson, S., Hagan, M., Mende, S., ... Paxton, L. (2006). Control of equatorial ionospheric morphology by atmospheric tides. *Geophysical Research Letters*, *33*(15). doi: 10.1029/2006GL026161

Leovy, C. B., & Zurek, R. W. (1979). Thermal tides and martian dust storms: Direct evidence for coupling. *Journal of Geophysical Research: Solid Earth*, *84*(B6), 2956–2968.

Liu, G., England, S., Lillis, R. J., Mahaffy, P. R., Elrod, M., Benna, M., & Jakosky, B. (2017). Longitudinal structures in mars' upper atmosphere as observed by maven/ngims. *Journal of Geophysical Research: Space Physics*, *122*(1), 1258–1268. doi: 10.1002/2016JA023455

Lo, D. Y., Yelle, R. V., Schneider, N. M., Jain, S. K., Stewart, A. I. F., England, S. L., ... others (2015). Nonmigrating tides in the martian atmosphere as observed by maven iuvs. *Geophysical Research Letters*, *42*(21), 9057–9063. doi: 10.1002/2015GL066268

Mahaffy, P. R., Benna, M., King, T., Harpold, D. N., Arvey, R., Barciniak, M., ... others (2015). The neutral gas and ion mass spectrometer on the mars atmosphere and volatile evolution mission. *Space Science Reviews*, *195*(1-4), 49–73. doi: 10.1007/s11214-014-0091-1

Montabone, L., Spiga, A., Kass, D. M., Kleinböhl, A., Forget, F., & Millour, E. (2020). Martian year 34 column dust climatology from mars climate sounder observations: Reconstructed maps and model simulations. *Journal of Geophys-*

ical Research: Planets. doi: 10.1029/2019JE006111

Moudden, Y., & Forbes, J. (2008). Topographic connections with density waves in mars' aerobraking regime. *Journal of Geophysical Research: Planets*, *113*(E11). doi: 10.1029/2008JE003107

Moudden, Y., & Forbes, J. (2010). A new interpretation of mars aerobraking variability: Planetary wave-tide interactions. *Journal of Geophysical Research: Planets*, *115*(E9). doi: 10.1029/2009JE003542

Němec, F., Morgan, D., Gurnett, D., Duru, F., & Truhlík, V. (2011). Dayside ionosphere of mars: Empirical model based on data from the marsis instrument. *Journal of Geophysical Research: Planets*, *116*(E7). doi: 10.1029/2010JE003789

Sakai, S., Andersson, L., Cravens, T. E., Mitchell, D. L., Mazelle, C., Rahmati, A., ... others (2016). Electron energetics in the martian dayside ionosphere: Model comparisons with maven data. *Journal of Geophysical Research: Space Physics*, *121*(7), 7049–7066.

Schunk, R., & Nagy, A. (2009). *Ionospheres: physics, plasma physics, and chemistry*. Cambridge university press.

Thaller, S. A., Andersson, L., Pilinski, M. D., Thiemann, E., Withers, P., Elrod, M., ... Jenkins, G. (2020). Tidal wave-driven variability in the mars ionosphere-thermosphere system. *Atmosphere*, *11*(5), 521. doi: 10.3390/atmos11050521

Wang, L., Fritts, D., & Tolson, R. (2006). Nonmigrating tides inferred from the mars odyssey and mars global surveyor aerobraking data. *Geophysical research letters*, *33*(23). doi: 10.1029/2006GL027753

Wilson, R. J. (2002). Evidence for nonmigrating thermal tides in the mars upper atmosphere from the mars global surveyor accelerometer experiment. *Geophysical research letters*, *29*(7), 24–1. doi: 10.1029/2001GL013975

Withers, P., Bougher, S., & Keating, G. (2003). The effects of topographically-controlled thermal tides in the martian upper atmosphere as seen by the mgs accelerometer. *Icarus*, *164*(1), 14–32. doi: 10.1016/S0019-1035(03)00135-0

Wu, Z., Li, T., & Dou, X. (2015). Seasonal variation of martian middle atmosphere tides observed by the mars climate sounder. *Journal of Geophysical Research: Planets*, *120*(12), 2206–2223. doi: 10.1002/2015JE004922

Zurek, R. W. (1976). Diurnal tide in the martian atmosphere. *Journal of the Atmo-*

spheric Sciences, *33*(2), 321–337.

References from Supporting Information

Ma, Y., Fang, X., Russell, C. T., Nagy, A. F., Toth, G., Luhmann, J. G., . . . Dong, C. (2014). Effects of crustal field rotation on the solar wind plasma interaction with mars. *Geophysical Research Letters, 41*(19), 6563-6569

Morschhauser, A., Lesur, V., & Grott, M. (2014). A spherical harmonic model of the lithospheric magnetic field of mars. *Journal of Geophysical Research: Planets, 119*(6), 1162-1188. doi: 10.1002/2013JE004555

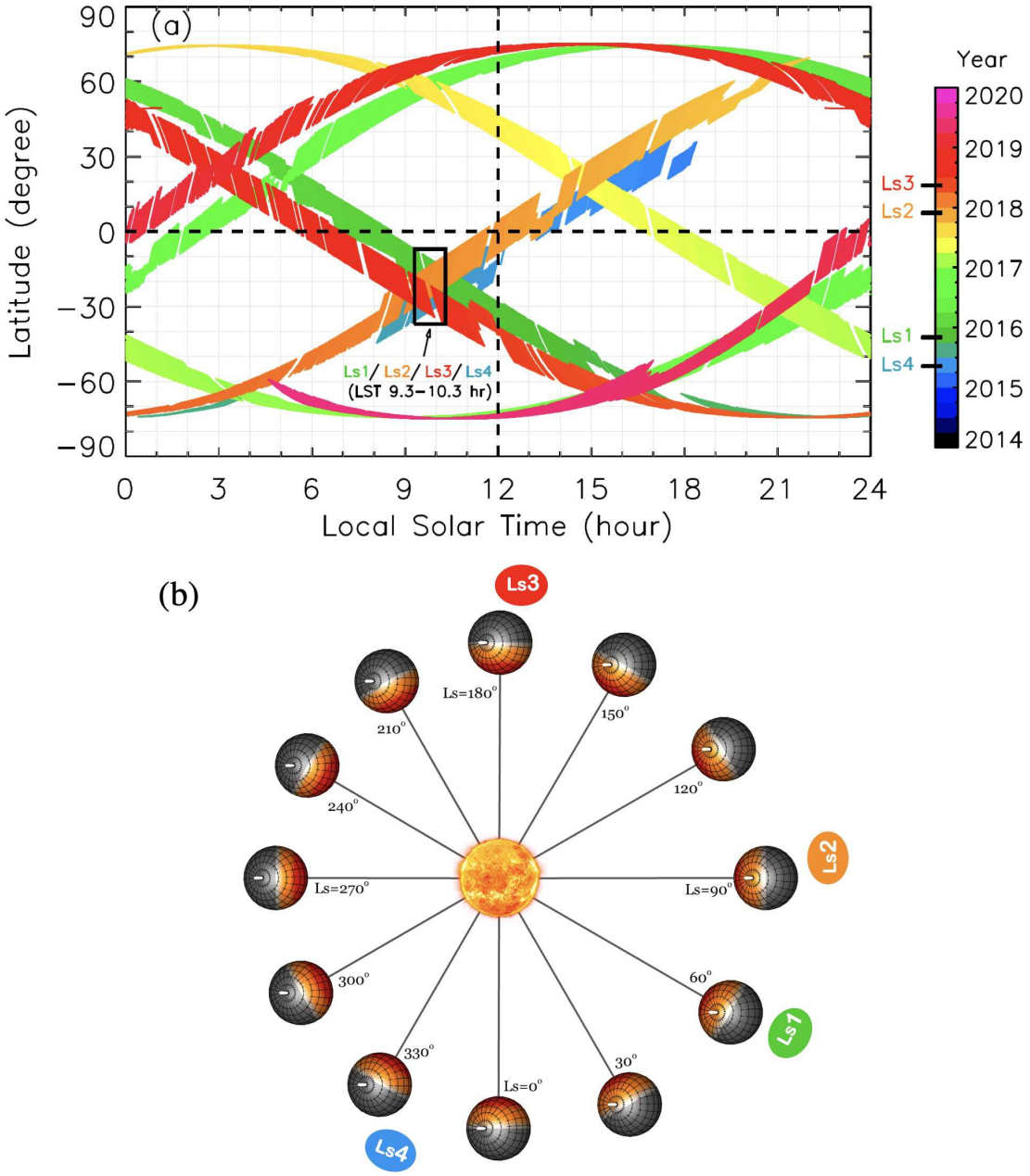

Figure 1. (a) MAVEN inbound orbits within 150-200 km altitudes projected onto the LT-latitude plane, whenever verified CO_2 density measurements are available from the NGIMS instrument. (b) Seasonal variation of Mars orbital positions with respect to the Sun. Their relative positions and Mars orientations are rigorously calculated using NAIF-SPICE. The planetary rotational axis is also shown (in white), demonstrating the seasonal change of the solar declination angle. Four time intervals for our case study (Ls1-Ls4, see Table 1), having compatible LT and latitudinal but different seasonal coverages, are marked in both panels.

Table 1. Four Cases of MAVEN Inbound Periapsis Passages Within 1-h Local Time Window of 9.3-10.3 and Below 200-km Altitude

Case	Ls (degree)	Time Interval	Mars Year	Latitude* (degree)	SZA* (degree)
Ls1	[60, 66]	[2015-10-25, 2015-11-08]	33	[-28.0, -6.9]	[44.0, 57.9]
Ls2	[91, 97]	[2017-11-22, 2017-12-05]	34	[-30.3, -9.4]	[43.0, 68.0]
Ls3	[173, 180]	[2018-05-10, 2018-05-22]	34	[-37.7, -17.5]	[37.3, 47.4]
Ls4	[336, 343]	[2015-05-04, 2015-05-16]	32	[-35.9, -16.7]	[26.0, 46.6]

Case	r_{SM}^{-2} † (AU^{-2})	EUVM-A§ 17-22 nm (mW/m^2)	EUVM-B§ 0-7 nm (mW/m^2)	EUVM-C§ 121.6 nm (mW/m^2)	$F_{10.7}^{\ddagger}$ at Mars (sfu)	sunspot number	dust†† optical depth
Ls1	0.361	0.262	0.273	2.763	39.7	82	0.07
Ls2	0.366	0.156	0.047	2.310	25.6	6	0.08
Ls3	0.460	0.185	0.032	2.800	33.6	7	0.20
Ls4	0.440	0.323	0.339	3.405	50.3	136	0.28

*Collective spatial coverage of the selected MAVEN NGIMS and LPW instrument data.

†r_{SM}^{-2} stands for the inverse square of the Sun-Mars distance.

§Energy flux of solar irradiance above the atmosphere in three EUVM wavelength channels.

‡$F_{10.7}$ index at Mars' orbit, which is extrapolated from Earth considering the change due to heliocentric distances and Earth-Sun-Mars angles.

††Average column dust optical depth at 9.3 μm, scaled to atmospheric pressure of 610 Pa.

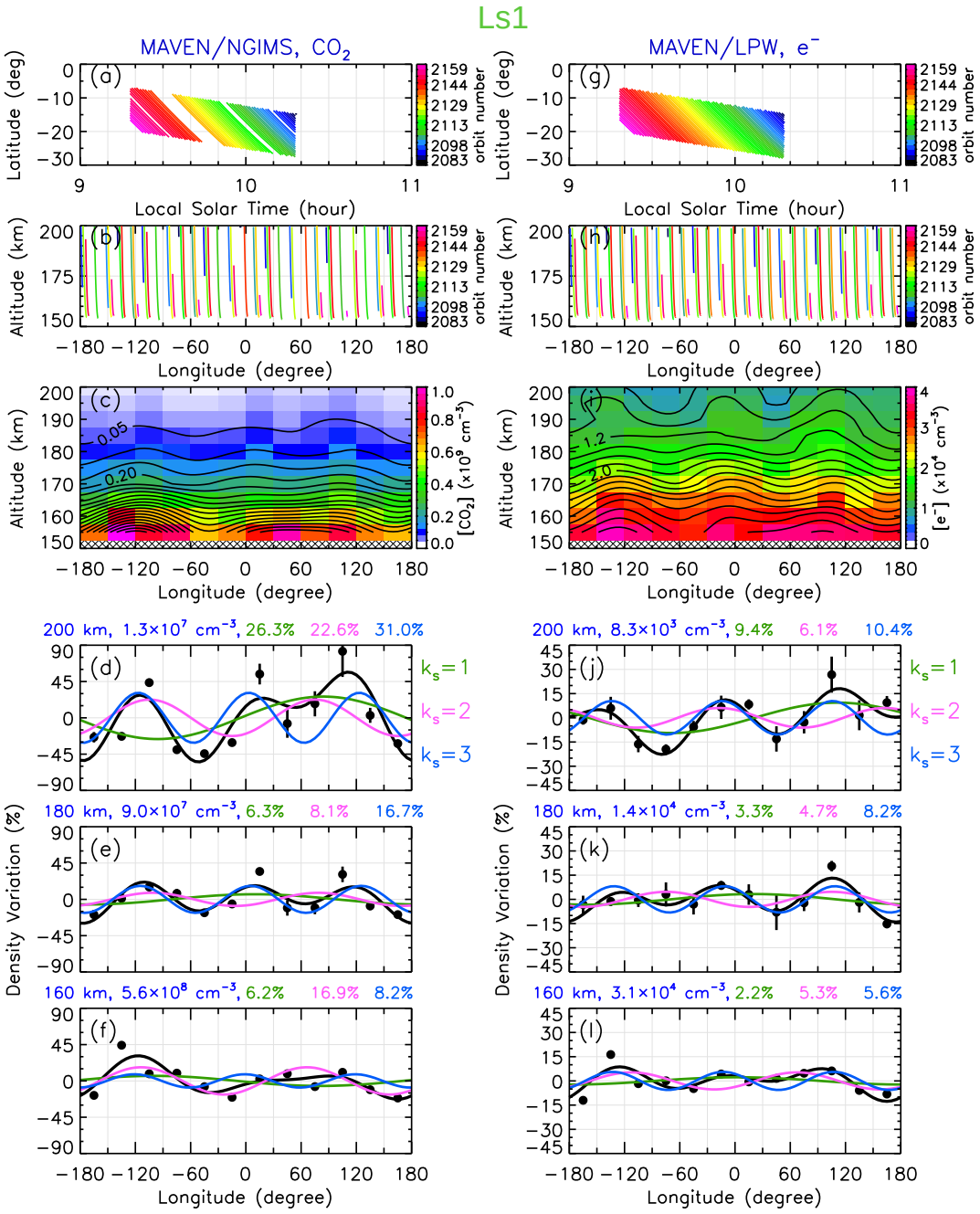

Figure 2. (left) MAVEN/NGIMS CO_2 density and (right) MAVEN/LPW electron density measurements in Ls1 and their longitude variations. The top two rows show the projection of the selected orbital data over the LT-latitude and longitude-altitude planes, respectively, color coded by MAVEN orbital number. The third row presents altitude-longitude structures, which are mean densities (in color) superposed by least squares composite k_s=1-3 spectral fits (black curves, spaced by 5×10^7 cm^{-3} for CO_2 and 2×10^3 cm^{-3} for electrons). The cross-hatched areas indicate no data. The bottom three rows show the density variation in percent with respect to the zonal average as a function of longitude at representative altitudes of 200 km, 180 km, and 160 km, respectively. The average values over individual longitude bins are shown as black dots, with error bars showing standard error of the mean. The curves show individual spectral fits (green, k_s=1; purple, k_s=2; blue, k_s=3) and the composite spectra (thick black). The zonal mean densities and wave amplitudes (in percent of the zonal means) are marked above each panel. Note that the scale of the Y axis in panels (j-l) is different from that in panels (d-f).

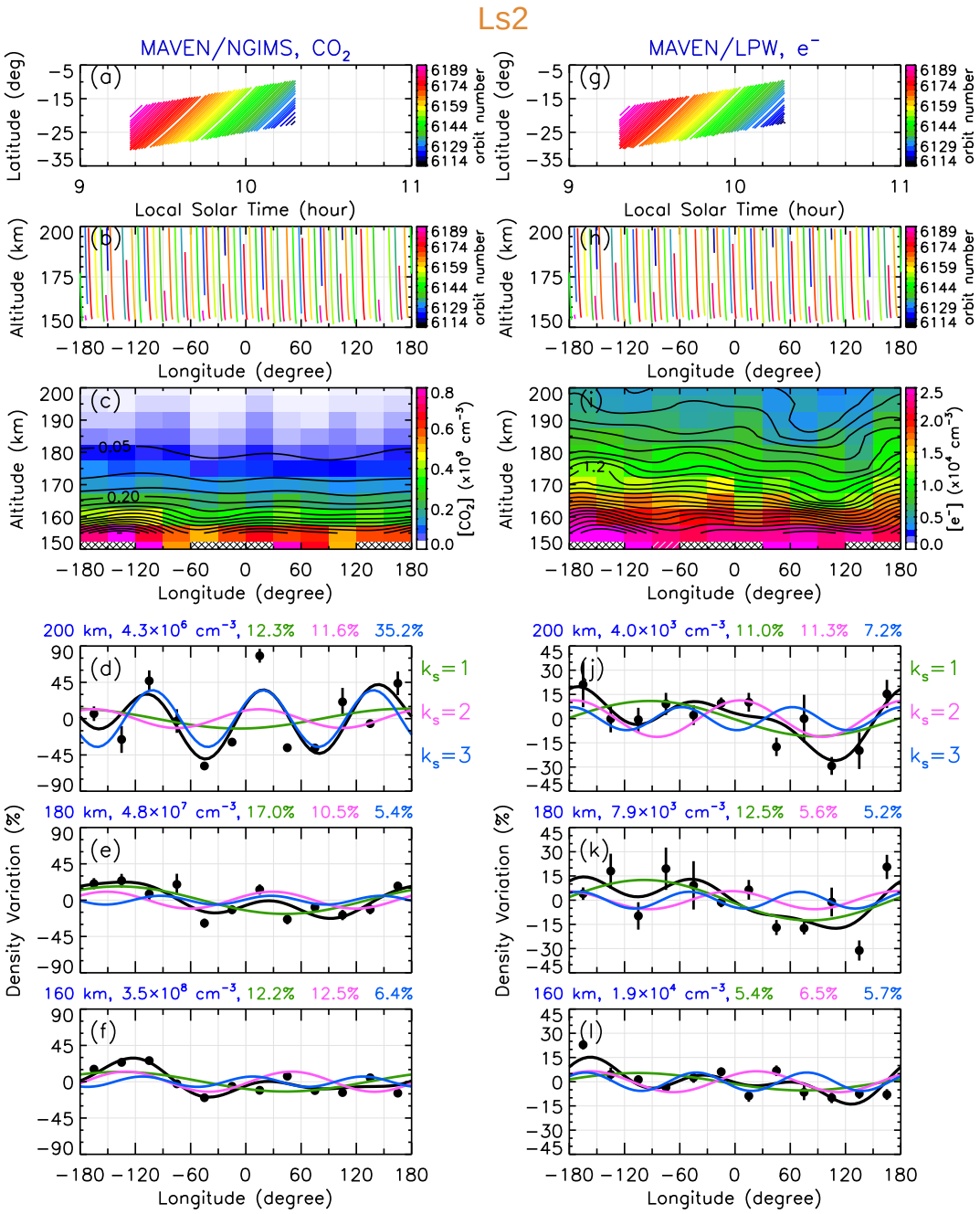

Figure 3. Similar to Figure 2 but for the case of Ls2. Note that white-hatched areas in longitude-altitude density structures indicate the bins where the number of available MAVEN data points for averaging is less than 5. In this case, such a low coverage bin exists near 150 km altitude and between the 60°-90°W longitudes. The contour lines in panels (c) and (i) are spaced by 5×10^7 and 10^3 cm^{-3}, respectively.

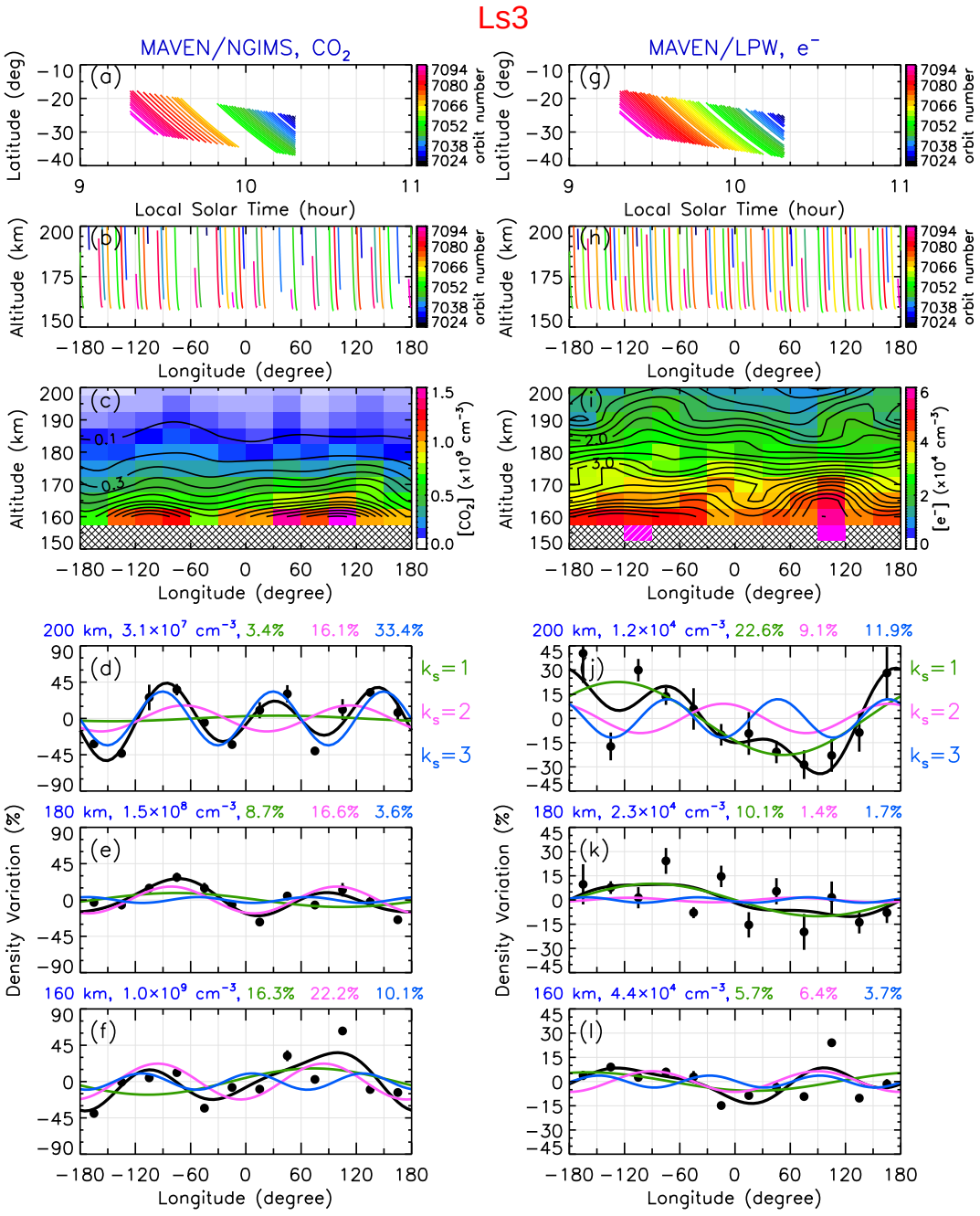

Figure 4. Similar to Figure 2 but for the case of Ls3. The contour lines in panels (c) and (i) are spaced by 10^8 and 2×10^3 cm^{-3}, respectively.

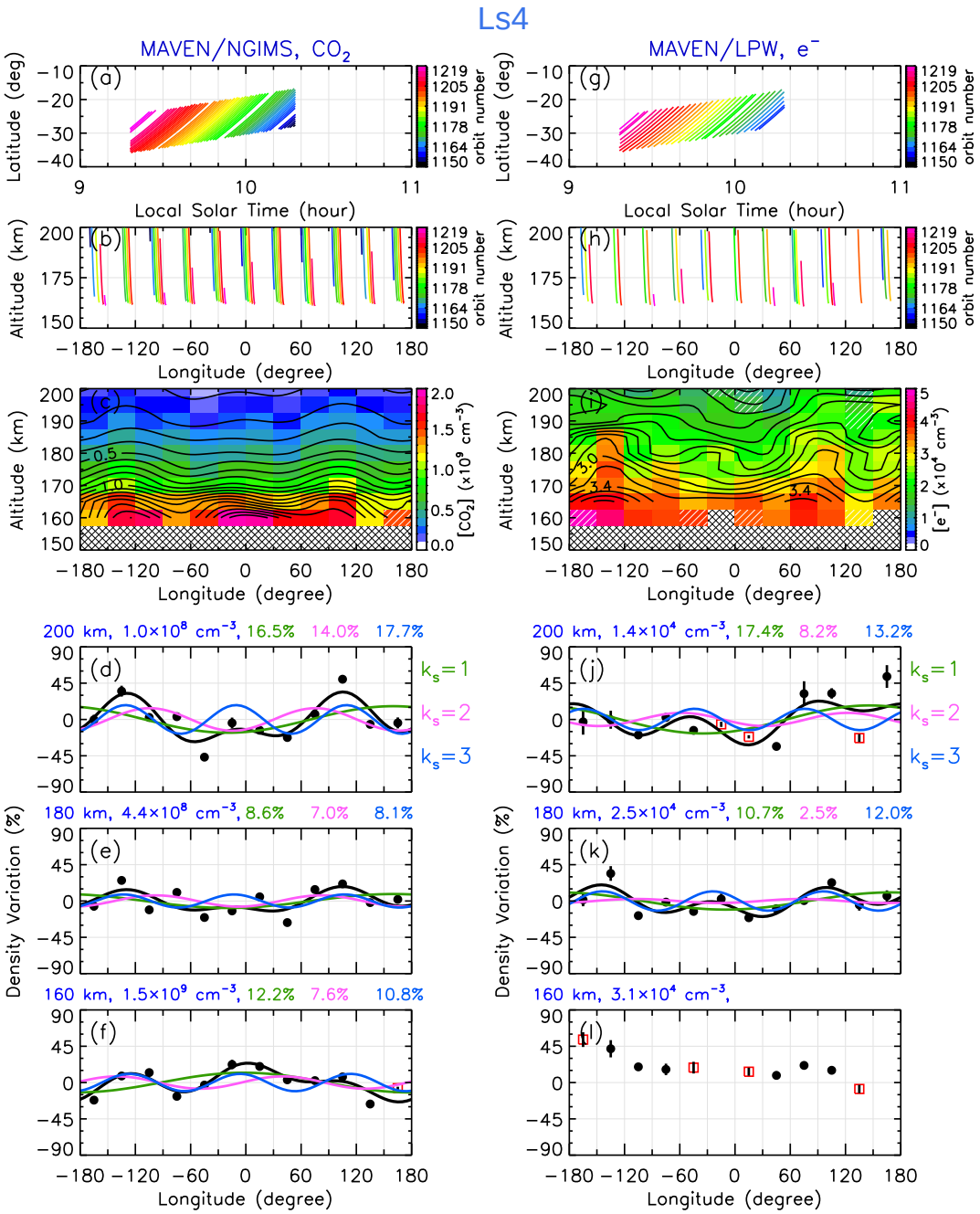

Figure 5. Similar to Figure 2 but for the case of Ls4. The contour lines in panels (c) and (i) are spaced by 10^8 and 2×10^3 cm^{-3}, respectively. In panels (f), (j) and (l), red squares represent the mean densities inside the longitude-altitude bins where the number of usable data points is less than 5. In panel (l), the least-squares spectral fit is not performed near 160 km altitude since not all longitude bins are sampled by MAVEN in this case. Note that unlike Figures 2-4, an identical Y-axis scale is used in panels (d-f) and (j-l) here.

Table 2. Summarized tidal structures of CO_2, O, N_2, Ar, and electron densities and electron temperature during Ls1-Ls4 at three respresentative altitudes (200 km, 180 km, 160 km)

CO_2 Density

		200 km altitude				180 km altitude				160 km altitude			
	H_n*	A_0†	A_1§	A_2§	A_3§	A_0	A_1	A_2	A_3	A_0	A_1	A_2	A_3
Case	(km)	(cm^{-3})	(%)	(%)	(%)	(cm^{-3})	(%)	(%)	(%)	(cm^{-3})	(%)	(%)	(%)
Ls1	11.0	$(1.3\pm0.1)\times10^7$	26.3±13.9	22.6±13.8	31.0±14.0	$(9.0\pm0.4)\times10^7$	6.3±6.9	8.1±6.9	16.7±7.0	$(5.6\pm0.3)\times10^8$	6.2±6.8	16.9±6.8	8.2±6.8
Ls2	9.4	$(4.3\pm0.5)\times10^6$	12.3±17.5	11.6±17.5	35.2±18.0	$(4.8\pm0.2)\times10^7$	17.0±6.9	10.5±6.9	5.4±6.8	$(3.5\pm0.1)\times10^8$	12.2±4.3	12.5±4.3	6.4±4.3
Ls3	11.2	$(3.1\pm0.1)\times10^7$	3.4±6.9	16.1±7.0	33.4±7.1	$(1.5\pm0.1)\times10^8$	8.7±4.8	16.6±4.8	3.6±4.8	$(1.0\pm0.1)\times10^9$	16.3±10.1	22.2±10.1	10.1±10.0
Ls4	14.6	$(1.0\pm0.1)\times10^8$	16.5±8.3	14.0±8.3	17.7±8.3	$(4.4\pm0.2)\times10^8$	8.6±7.7	7.0±7.7	8.1±7.7	$(1.5\pm0.1)\times10^9$	12.2±5.1	7.6±5.1	10.8±5.1

O Density

		200 km altitude				180 km altitude				160 km altitude			
	H_n*	A_0†	A_1§	A_2§	A_3§	A_0	A_1	A_2	A_3	A_0	A_1	A_2	A_3
Case	(km)	(cm^{-3})	(%)	(%)	(%)	(cm^{-3})	(%)	(%)	(%)	(cm^{-3})	(%)	(%)	(%)
Ls1	20.4	$(1.0\pm0.04)\times10^7$	21.5±5.6	19.9±5.6	11.5±5.5	$(2.7\pm0.1)\times10^7$	17.3±6.4	19.1±6.4	9.7±6.3	$(7.4\pm0.4)\times10^7$	9.2±7.4	30.0±7.5	6.0±7.4
Ls2	18.7	$(5.1\pm0.2)\times10^6$	13.7±6.4	22.7±6.4	9.0±6.4	$(1.5\pm0.1)\times10^7$	12.6±6.9	16.2±6.9	6.9±6.8	$(4.3\pm0.2)\times10^7$	8.2±5.6	11.8±5.6	12.7±5.6
Ls3	18.7	$(1.3\pm0.1)\times10^7$	18.9±6.7	23.1±6.7	20.5±6.7	$(3.3\pm0.3)\times10^7$	32.8±12.4	20.6±12.2	27.4±12.3	$(1.1\pm0.1)\times10^8$	31.7±10.5	21.4±10.3	14.4±10.3
Ls4	22.4	$(1.4\pm0.1)\times10^7$	21.9±6.2	13.9±6.2	19.9±6.2	$(3.4\pm0.1)\times10^7$	17.9±5.3	10.9±5.3	16.8±5.3	$(8.2\pm0.5)\times10^7$	11.2±7.8	10.4±7.8	16.6±7.8

Table 2. (Cont'd)

N_2 Density

		200 km altitude				180 km altitude				160 km altitude			
	H_n*	A_0†	A_1§	A_2§	A_3§	A_0	A_1	A_2	A_3	A_0	A_1	A_2	A_3
Case	(km)	(cm^{-3})	(%)	(%)	(%)	(cm^{-3})	(%)	(%)	(%)	(cm^{-3})	(%)	(%)	(%)
Ls1	18.1	$(7.5\pm0.4)\times10^6$	17.5±7.0	10.5±6.9	16.5±7.0	$(2.3\pm0.1)\times10^7$	11.6±4.8	10.1±4.8	9.1±4.8	$(7.1\pm0.3)\times10^7$	5.9±5.4	21.7±5.5	3.6±5.4
Ls2	16.6	$(4.5\pm0.3)\times10^6$	6.4±7.9	14.8±8.0	11.6±7.9	$(1.6\pm0.1)\times10^7$	12.1±5.5	10.4±5.5	3.0±5.5	$(5.2\pm0.2)\times10^7$	6.6±4.8	8.8±4.8	5.5±4.8
Ls3	17.4	$(1.3\pm0.1)\times10^7$	7.3±5.5	11.3±5.5	16.9±5.5	$(3.6\pm0.2)\times10^7$	18.3±7.3	13.1±7.3	12.1±7.3	$(1.3\pm0.1)\times10^8$	12.7±9.9	21.2±10.0	10.5±9.9
Ls4	22.7	$(1.7\pm0.1)\times10^7$	18.6±5.8	11.5±5.7	15.8±5.8	$(4.4\pm0.2)\times10^7$	13.9±5.7	6.0±5.6	10.2±5.6	$(9.8\pm0.3)\times10^7$	6.5±4.5	6.6±4.5	8.8±4.5

Ar Density

		200 km altitude				180 km altitude				160 km altitude			
	H_n*	A_0†	A_1§	A_2§	A_3§	A_0	A_1	A_2	A_3	A_0	A_1	A_2	A_3
Case	(km)	(cm^{-3})	(%)	(%)	(%)	(cm^{-3})	(%)	(%)	(%)	(cm^{-3})	(%)	(%)	(%)
Ls1	13.5	$(9.2\pm0.7)\times10^5$	–‡	–	–	$(3.0\pm0.1)\times10^6$	7.4±6.6	8.4±6.6	14.3±6.6	$(1.5\pm0.1)\times10^7$	4.7±6.1	17.8±6.1	5.6±6.1
Ls2	12.9	–	–	–	–	$(1.9\pm0.1)\times10^6$	14.5±4.9	7.1±4.9	2.1±4.9	$(9.8\pm0.3)\times10^6$	10.7±4.5	11.3±4.5	3.5±4.5
Ls3	12.6	$(1.5\pm0.1)\times10^6$	3.9±7.6	16.1±7.6	21.5±7.6	$(5.8\pm0.2)\times10^6$	11.3±4.8	15.5±4.8	5.7±4.8	$(3.3\pm0.2)\times10^7$	9.8±9.3	21.4±9.4	9.3±9.3
Ls4	16.2	$(3.1\pm0.2)\times10^6$	16.5±7.4	12.6±7.4	17.1±7.4	$(1.1\pm0.1)\times10^7$	10.0±6.7	5.7±6.7	8.2±6.7	$(3.5\pm0.1)\times10^7$	10.1±4.1	4.5±4.1	7.2±4.1

Table 2. (Cont'd)

e$^-$ Density

		200 km altitude				180 km altitude				160 km altitude			
	H_e*	A_0†	A_1§	A_2§	A_3§	A_0	A_1	A_2	A_3	A_0	A_1	A_2	A_3
Case	(km)	(cm^{-3})	(%)	(%)	(%)	(cm^{-3})	(%)	(%)	(%)	(cm^{-3})	(%)	(%)	(%)
Ls1	29.4	(8.3±0.2)×10^3	9.4±3.7	6.1±3.7	10.4±3.7	(1.4±0.03)×10^4	3.3±2.9	4.7±2.9	8.2±2.9	(3.1±0.1)×10^4	2.2±2.8	5.3±2.8	5.6±2.8
Ls2	25.0	(4.0±0.1)×10^3	11.0±4.9	11.3±4.9	7.2±4.9	(7.9±0.4)×10^3	12.5±7.4	5.6±7.4	5.2±7.4	(1.9±0.05)×10^4	5.4±3.5	6.5±3.5	5.7±3.5
Ls3	28.9	(1.2±0.1)×10^4	22.6±7.1	9.1±7.0	11.9±7.0	(2.3±0.1)×10^4	10.1±6.6	1.4±6.6	1.7±6.6	(4.4±0.2)×10^4	5.7±4.8	6.4±4.8	3.7±4.8
Ls4	40.0	(1.4±0.1)×10^4	17.4±12.1	8.2±12.1	13.2±12.1	(2.5±0.1)×10^4	10.7±6.3	2.5±6.3	12.0±6.3	(3.1±0.5)×10^4	–‡	–	–

e$^-$ Temperature

		200 km altitude				180 km altitude				160 km altitude			
	H_{Te}*	A_0†	A_1§	A_2§	A_3§	A_0	A_1	A_2	A_3	A_0	A_1	A_2	A_3
Case	(km)	(K)	(%)	(%)	(%)	(K)	(%)	(%)	(%)	(K)	(%)	(%)	(%)
Ls1	-70.4	(1.8±0.03)×10^3	2.8±2.2	1.9±2.2	4.5±2.2	(1.4±0.01)×10^3	3.2±0.9	2.2±0.9	4.7±0.9	(1.0±0.01)×10^3	2.0±0.8	2.2±0.8	1.2±0.8
Ls2	-63.7	(1.6±0.04)×10^3	4.2±3.3	2.2±3.3	4.6±3.3	(1.2±0.02)×10^3	4.2±2.8	4.2±2.8	1.1±2.8	(8.7±0.1)×10^2	3.5±1.0	1.5±1.0	0.2±1.0
Ls3	-65.8	(1.3±0.01)×10^3	3.6±1.6	5.7±1.6	4.1±1.6	(9.4±0.1)×10^2	3.0±2.3	3.3±2.3	3.8±2.3	(7.0±0.1)×10^2	1.9±1.2	2.3±1.2	1.5±1.2
Ls4	-76.6	(1.4±0.1)×10^3	2.5±7.4	5.5±7.4	6.6±7.4	(9.9±0.1)×10^2	3.5±1.9	4.2±1.9	4.8±1.9	(7.3±1.2)×10^2	–	–	–

*Average scale height of the zonal mean altitude profile between 150-200 km altitudes.

†Zonal mean values.

§Relative wave amplitude with respect to the zonal mean for wavenumbers k_s=1, 2, 3

‡Wave fits are not performed when there is a lack of complete longitudinal coverage at given altitudes.

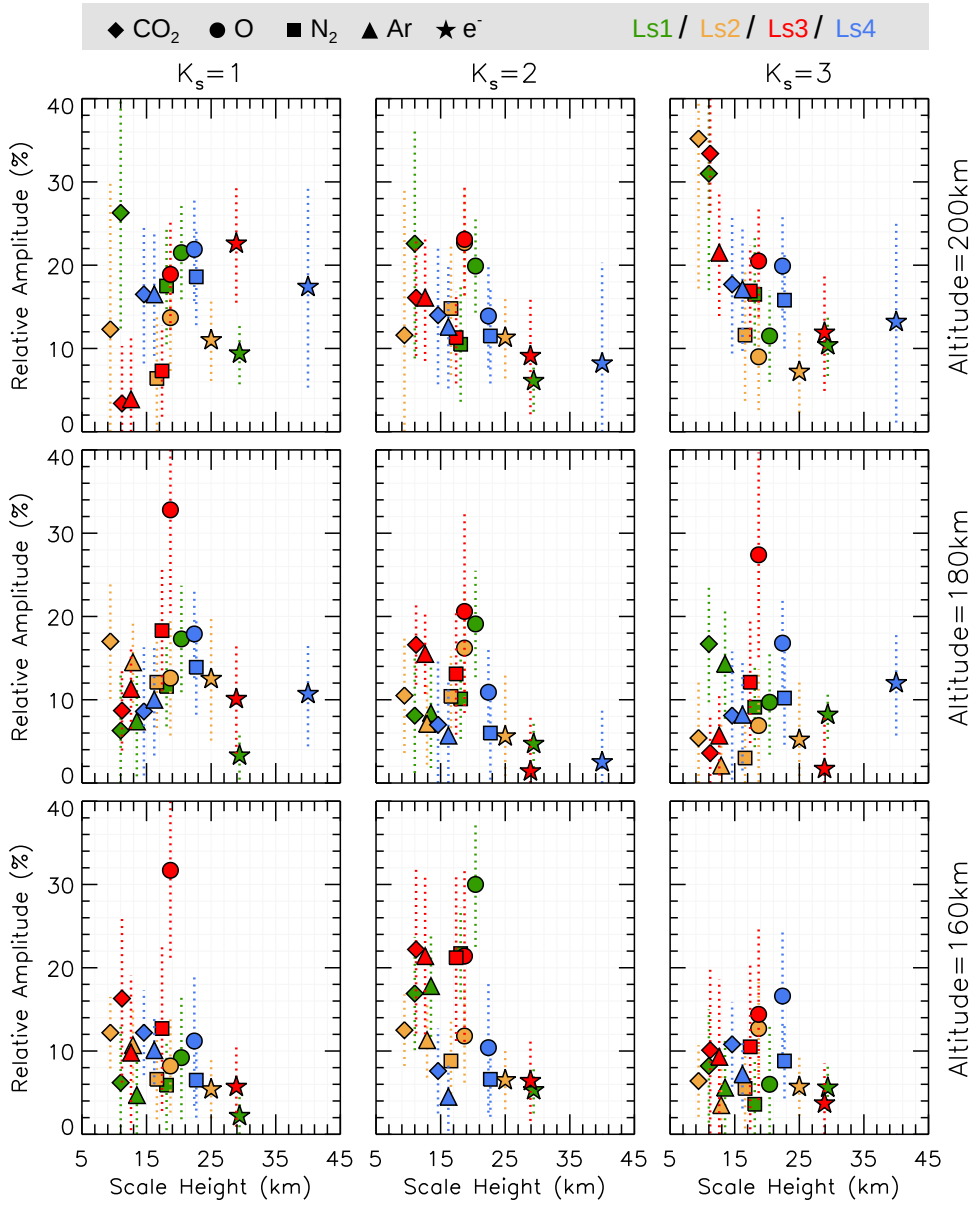

Figure 6. Relative wave amplitude (with respect to the zonal mean) versus the mean scale height. The results are shown for (from left to right) wavenumbers k_s=1, 2, and 3, and at three representative altitudes of (from top to bottom) 200 km, 180 km, and 160 km. As marked in the legend at the top, different symbols stand for different species, and different colors indicate different cases (Ls1-Ls4). The vertical dashed lines represent the uncertainty of the wave amplitudes.

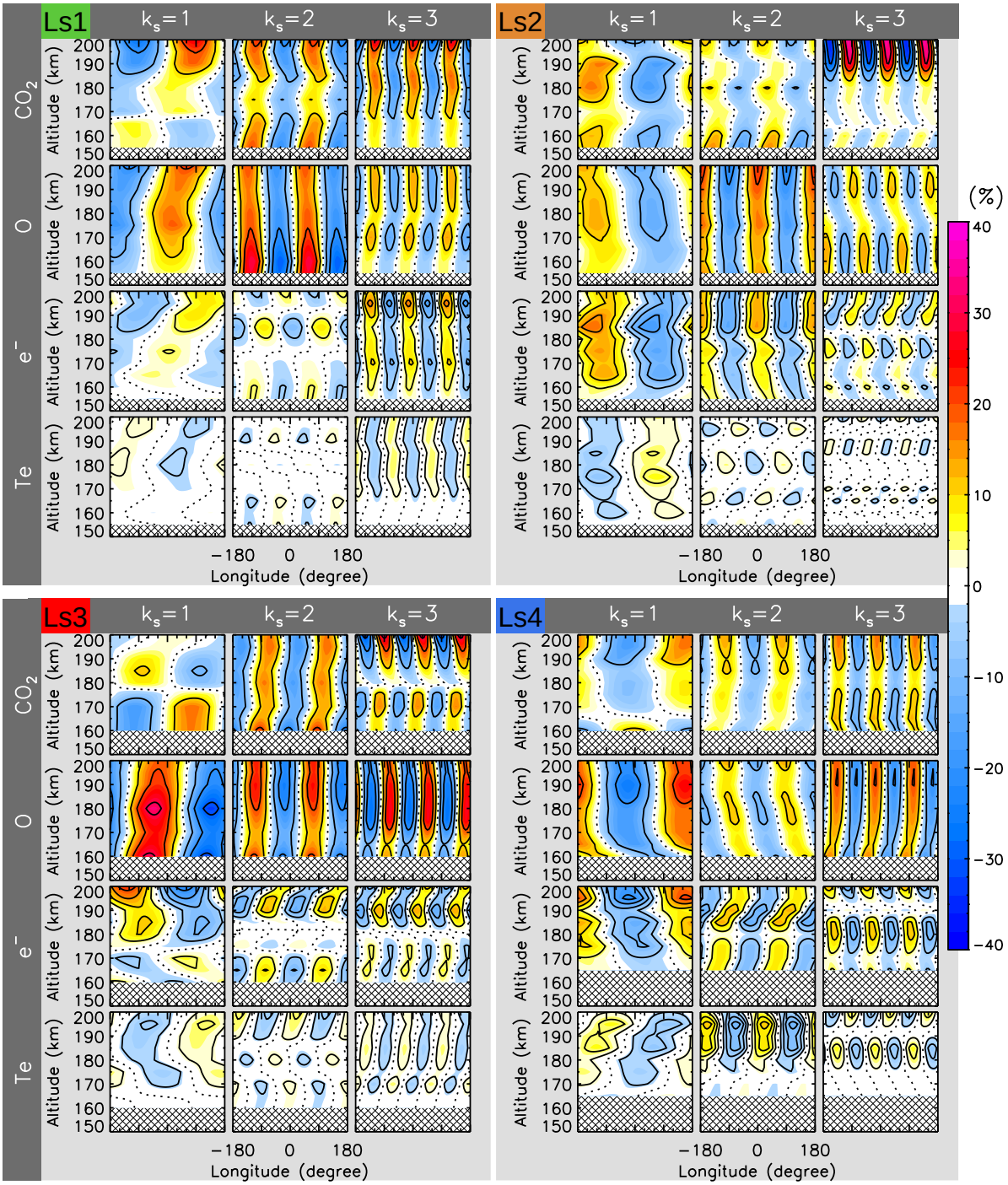

Figure 7. Comparison of wave decomposition of thermospheric and ionospheric tidal signatures among the four cases, with the group of panels in the upper left, upper right, bottom left, and bottom right for Ls1, Ls2, Ls3, and Ls4, respectively. In each case, the results are shown as zonal variation vs. altitude, after being normalized by the zonal means. Shown here are the tidal mode decomposition results for wavenumbers of (from left to right) k_s=1, 2, and 3, and for (from top to bottom) CO_2 density, O density, electron density, and electron temperature. The contour lines for the thermospheric tidal structures are spaced by 10%, and the contour lines for the ionospheric electron density and temperature are spaced by 5% and 2.5%, respectively. The dotted lines represent the contour level of 0.

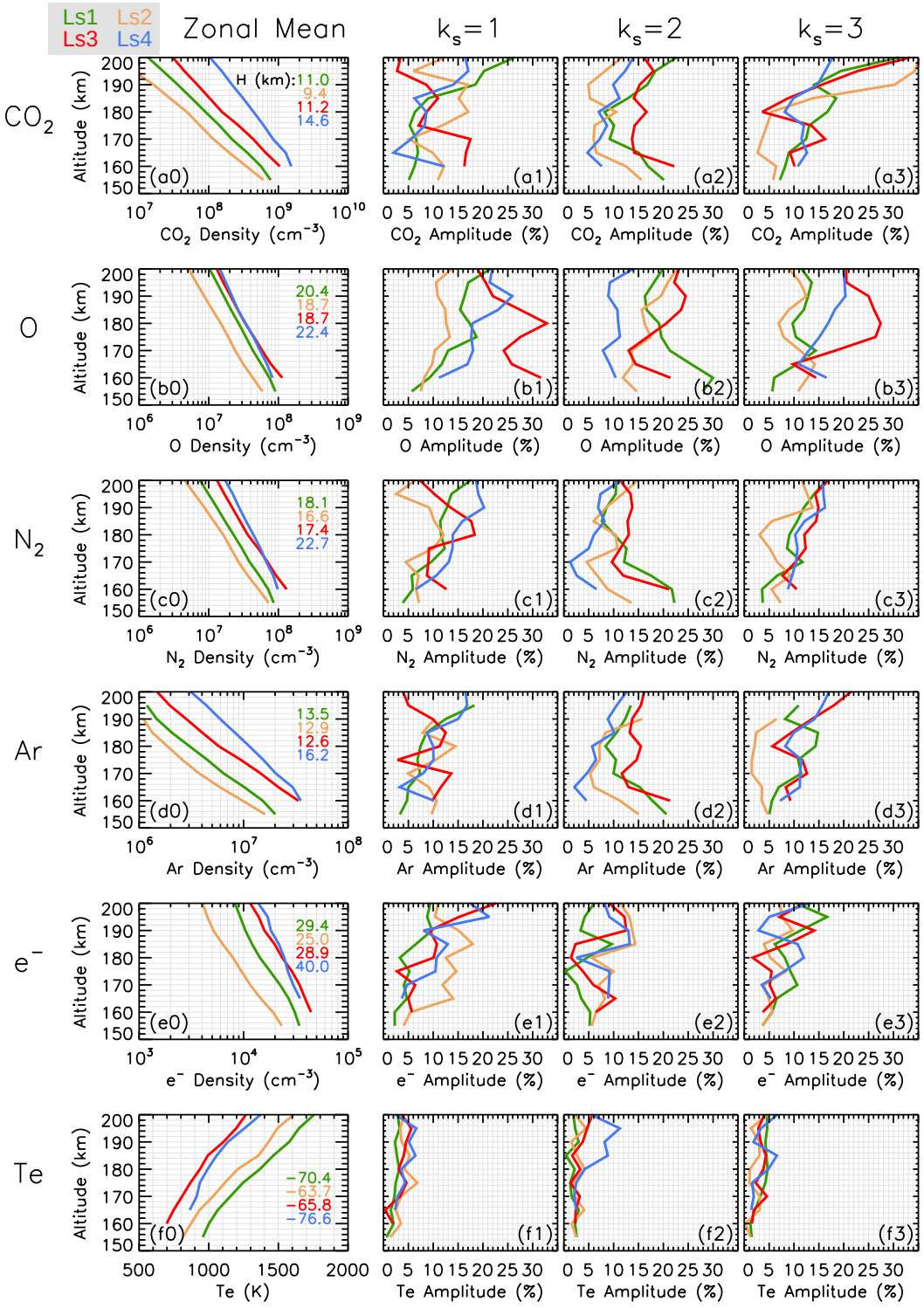

Figure 8. (from left to right) zonal means and tidal amplitudes of wavenumbers 1-3 as a function of altitude. The tidal amplitudes have been normalized by the zonal means. The results are shown for (from top to bottom) CO_2, O, N_2, Ar, and electron densities, and electron temperature. The curve colors of green/yellow/red/blue indicate the four cases of Ls1/Ls2/Ls3/Ls4, respectively. The mean scale heights, which are derived from the zonal mean distributions, are presented in the left column.

Table 3. Tidal Contributions to the Variability of Total Mass Density at 172 km Altitude as Predicted by the MCD (Retrieved from the Work of Forbes et al., 2020)

Case	A_1	A_2	A_3
Ls1	SPW1 (3%)	DE1 (13%), SPW2 (4%)	DE2 (12%), SE1 (4%), SPW3 (5%)
Ls2	SPW1 (3%)	DE1 (13%), SPW2 (4%)	DE2 (16%), SE1 (4%), SPW3 (6%)
Ls3	D0 (7%)	DE1 (6%), SPW2 (2%)	DE2 (15%), SE1 (4%), SPW3 (3%)
Ls4	SPW1 (3%), D0 (5%)	DE1 (7%), SPW2 (4%), S0 (4%)	DE2 (12%), SE1 (4%), SPW3 (4%)

Figure 1.

(a)

Latitude (degree)

90
60
30
0
−30
−60
−90

0 3 6 9 12 15 18 21 24

Local Solar Time (hour)

Ls1/ Ls2/ Ls3/ Ls4
(LST 9.3–10.3 hr)

Year
2020
2019
2018
2017
2016
2015
2014
Ls3
Ls2
Ls1
Ls4

(b)

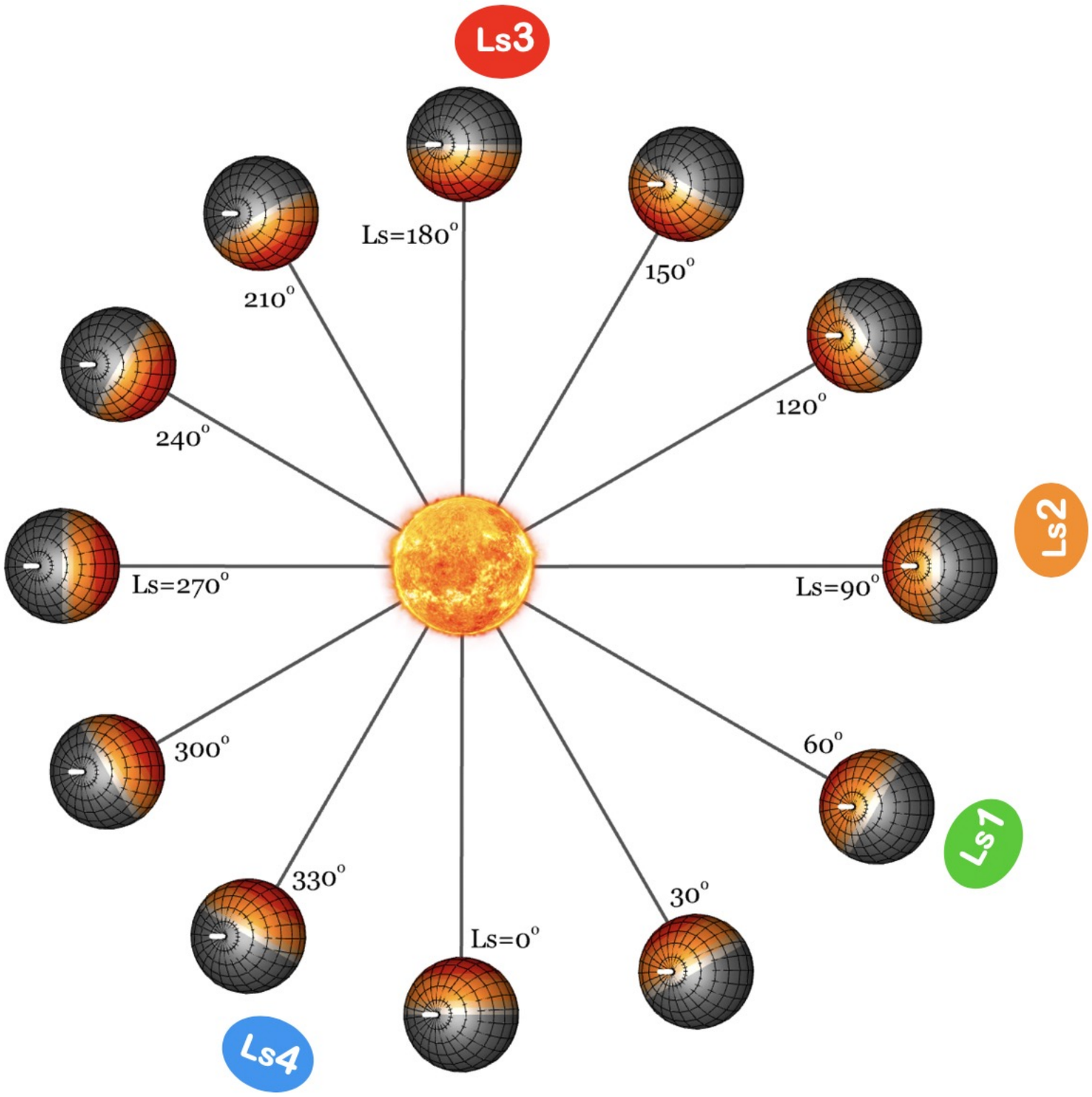

Figure 2.

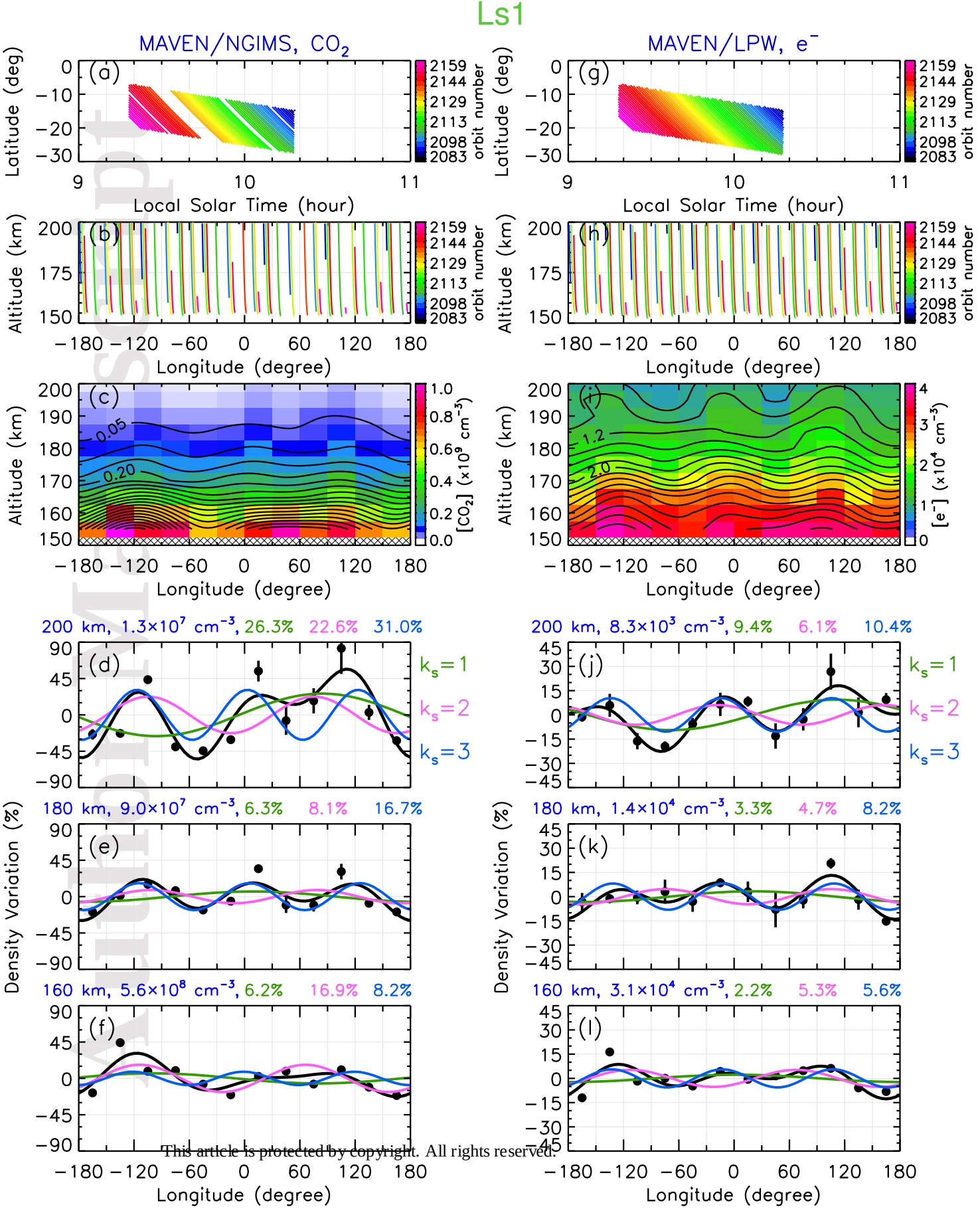

Figure 3.

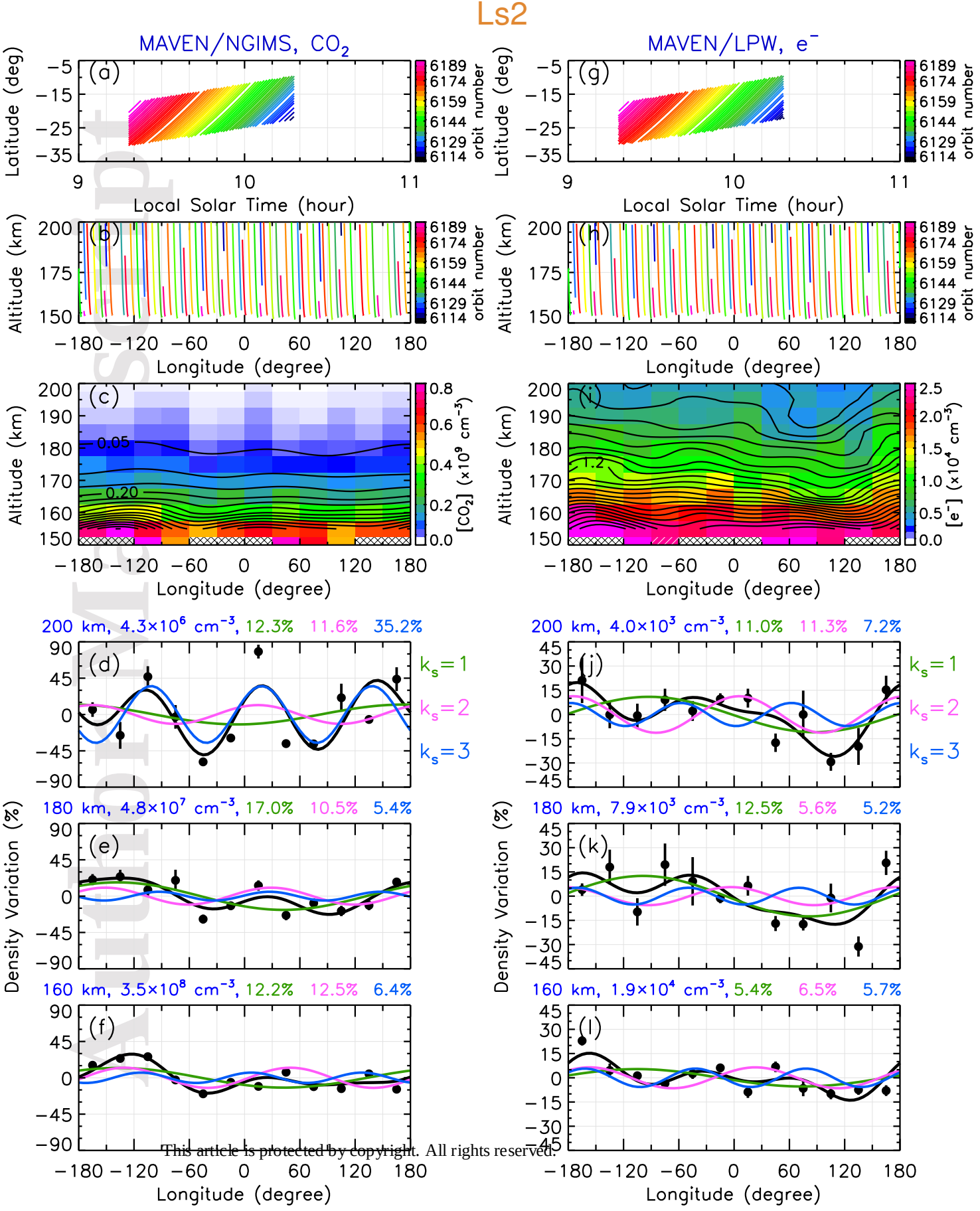

Figure 4.

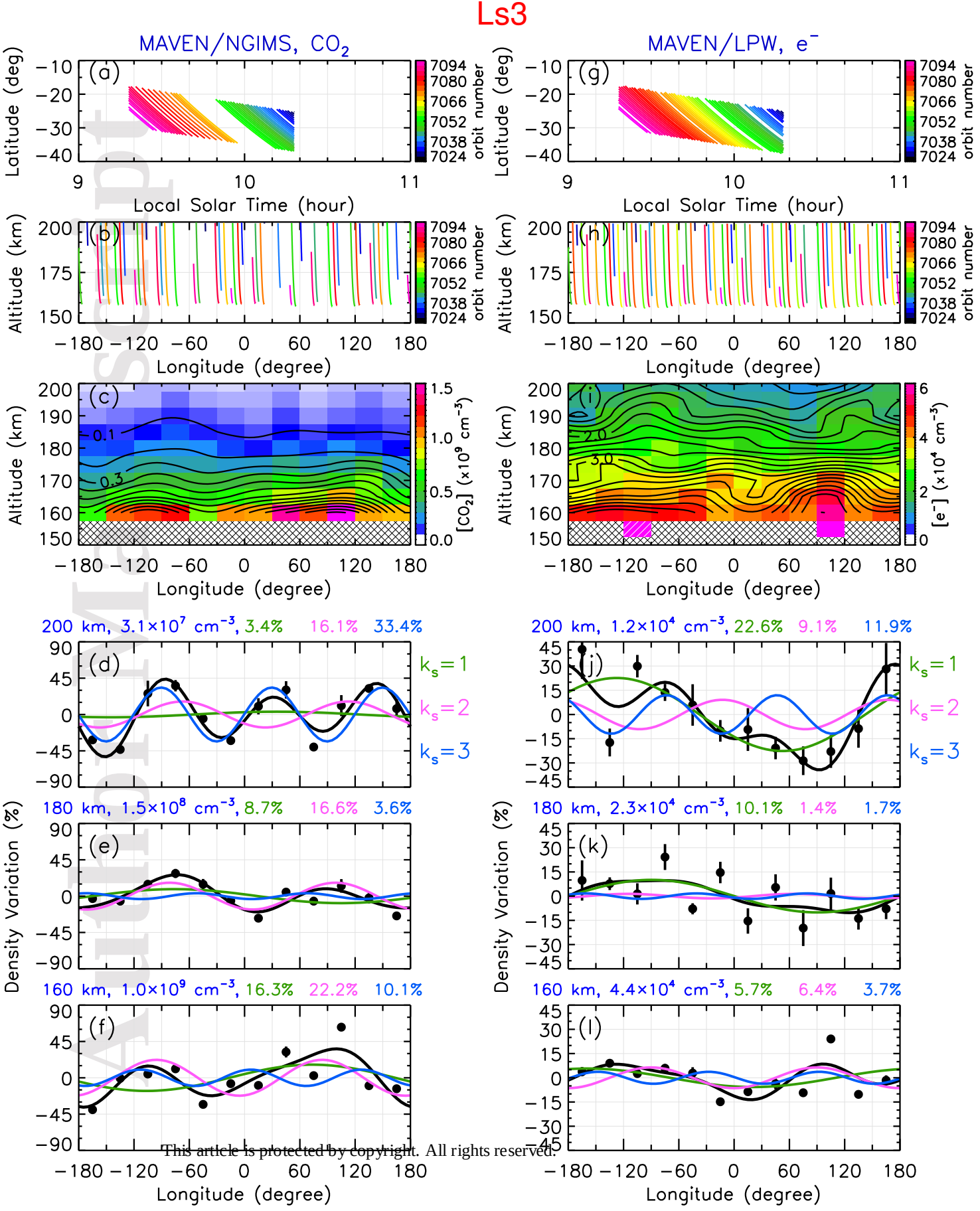

Figure 5.

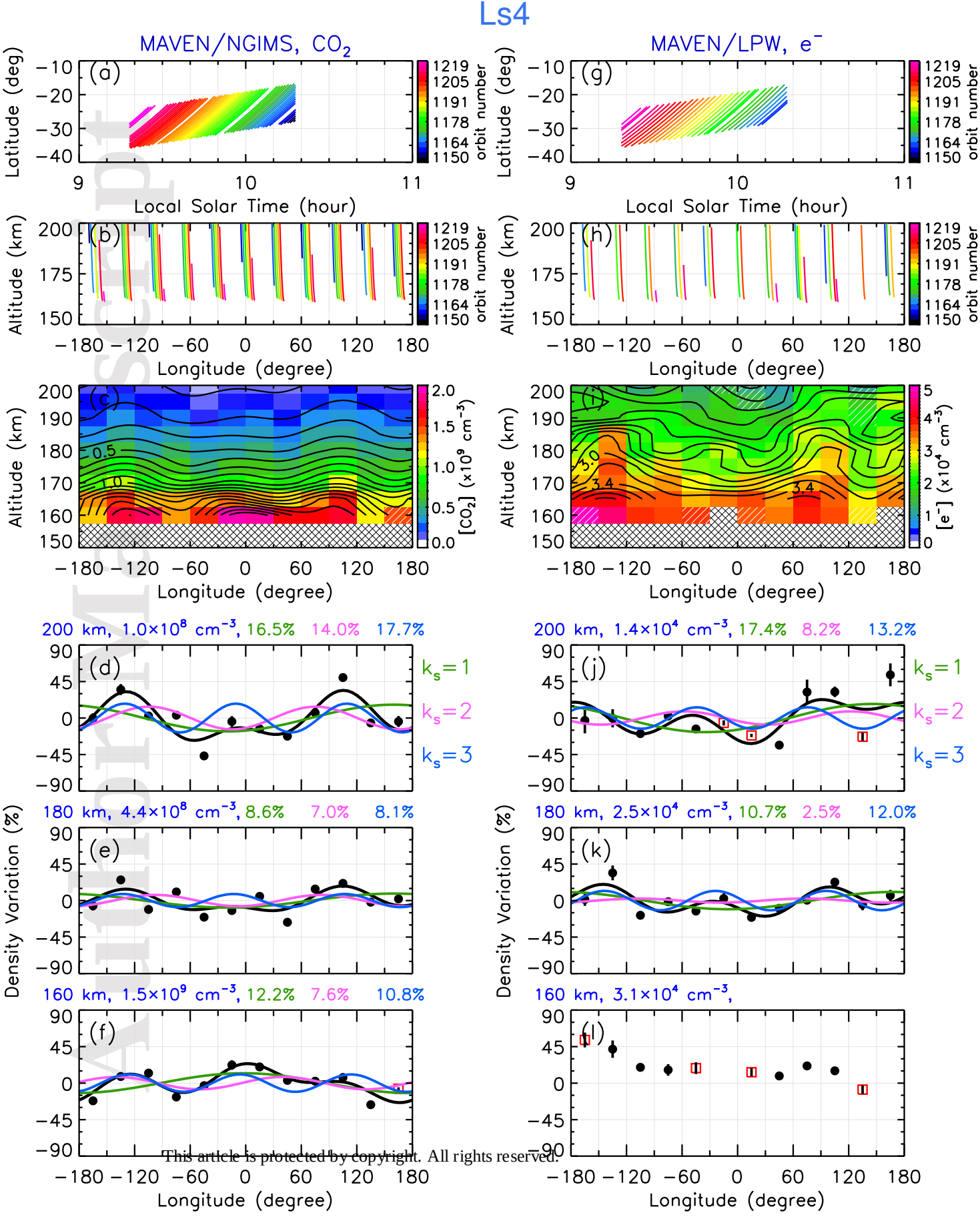

Figure 6.

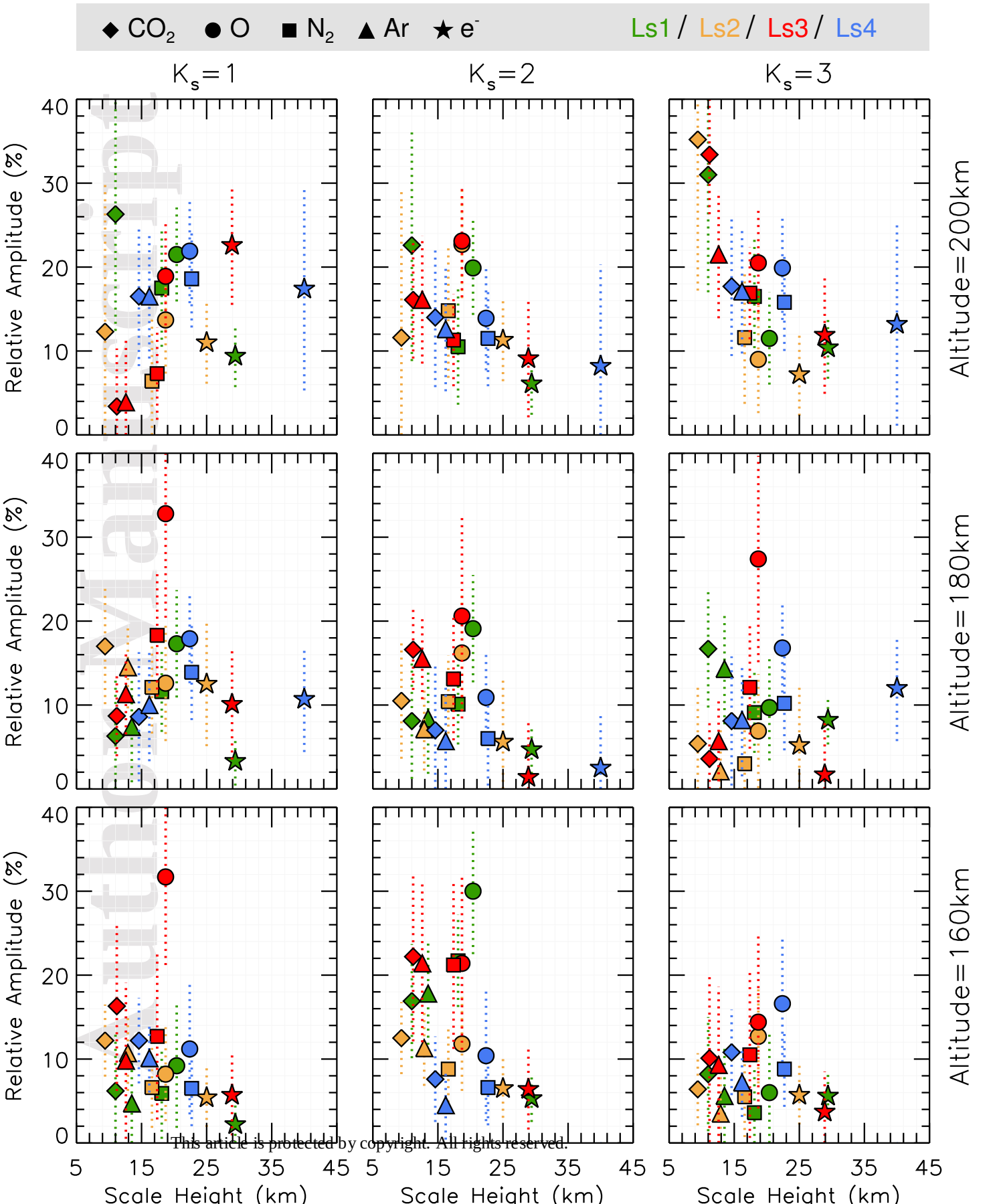

Figure 7.

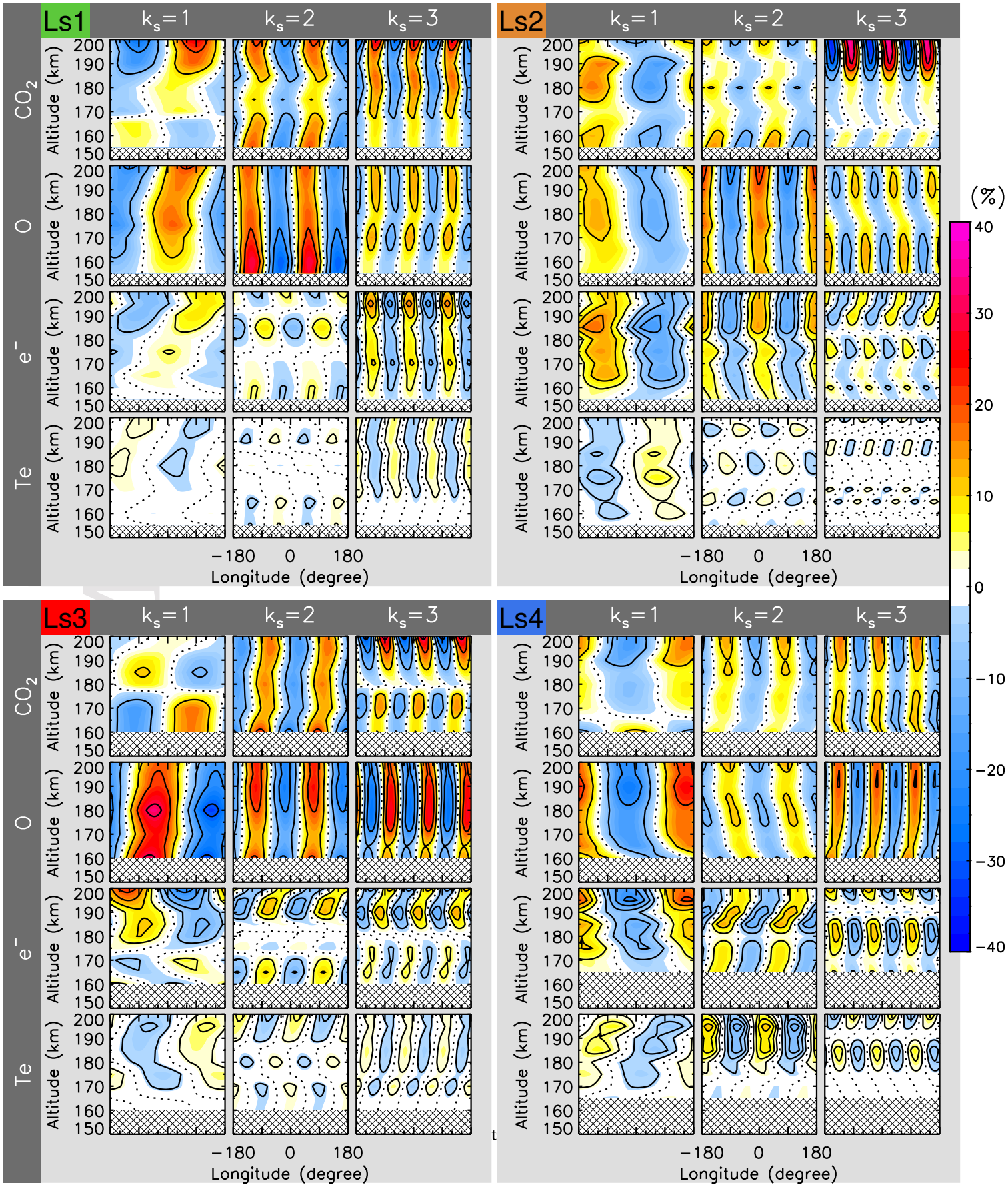
Ls1
Ls2
Ls3
Ls4
$k_s=1$
$k_s=2$
$k_s=3$
CO_2
O
e^-
Te
Altitude (km)
150
160
170
180
190
200
−180
0
180
Longitude (degree)
(%)
40
30
20
10
0
−10
−20
−30
−40

Figure 8.